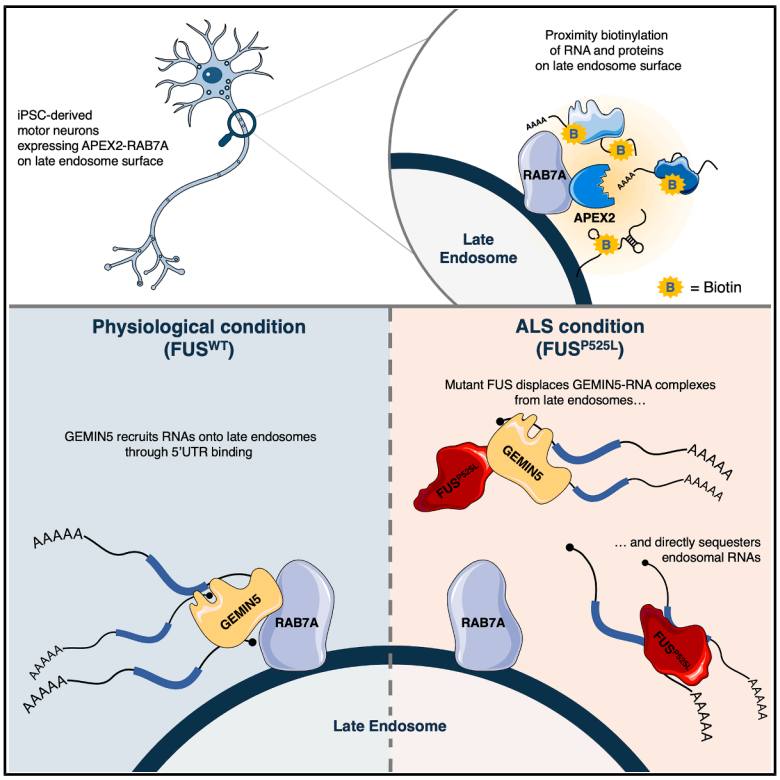
Cell Reports

Article

ALS-linked FUS mutation impairs GEMIN5-dependent mRNA recruitment to neuronal late endosomes

Graphical abstract



Highlights

- Specific neuronal and endosomal mRNAs are enriched on late endosomes in human motor neurons
- Conserved 5′UTR sequences are sufficient to target transcripts to late endosomes
- GEMIN5 binds the 5′UTRs of endosome-enriched RNAs and recruits them onto these vesicles
- ALS-linked FUS^{P525L} mutation sequesters GEMIN5 and mislocalizes endosomal transcripts

Authors

Adriano Setti, Lorenzo Stufera Mecarelli, Tiziana Santini, ..., Julie Martone, Davide Mariani, Irene Bozzoni

Correspondence

davide.mariani@uniroma1.it (D.M.), irene.bozzoni@uniroma1.it (I.B.)

In brief

Setti, Stufera Mecarelli et al. report that RAB7A-positive endosomes selectively load mRNAs enriched for axonal-synaptic functions in motor neurons. This process is mediated by GEMIN5, which promotes endosomal recruitment by binding 5′UTR sequences. Endosome-mediated RNA transport is disrupted by the ALS-associated FUS^{P525L} mutation, highlighting a novel vulnerable axis in neurodegeneration.

Setti et al., 2026, Cell Reports *45*, 118206
November 24, 2026 © 2026 The Authors. Published by Elsevier Inc.
https://doi.org/10.1016/j.celrep.2026.118206

CellPress

Cell Reports

CellPress
OPEN ACCESS

Article

ALS-linked FUS mutation impairs GEMIN5-dependent mRNA recruitment to neuronal late endosomes

Adriano Setti,[1,7] Lorenzo Stufera Mecarelli,[2,7] Tiziana Santini,[1] Angelo D'Angelo,[1] Vittorio Padovano,[1] Erika Vitiello,[3] Francesco Castagnetti,[4] Julie Martone,[5] Davide Mariani,[1,2,6,*] and Irene Bozzoni[1,2,6,8,*]

[1]Department of Biology and Biotechnology "Charles Darwin", Sapienza University of Rome, 00185 Rome, Italy
[2]Center for Human Technologies, Fondazione Istituto Italiano di Tecnologia (IIT), 16152 Genoa, Italy
[3]Institut für Pharmazie und Molekulare Biotechnologie, Universität Heidelberg, 69102 Heidelberg, Germany
[4]Karlsruher Institute für Technologie (KIT), 76131 Karlsruhe, Germany
[5]Institute of Molecular Biology and Pathology, National Research Council of Italy, 00185 Rome, Italy
[6]Center for Life Nano- & Neuro-Science@Sapienza, Fondazione Istituto Italiano di Tecnologia (IIT), 00161 Rome, Italy
[7]These authors contributed equally
[8]Lead contact
*Correspondence: davide.mariani@uniroma1.it (D.M.), irene.bozzoni@uniroma1.it (I.B.)
https://doi.org/10.1016/j.celrep.2026.118206

SUMMARY

Neurons depend on tightly regulated positioning of cellular components to maintain long-distance signaling, but the mechanisms guiding specific mRNAs to distant regions remain unclear. Here, we show that late endosomes function as selective RNA carriers in human motor neurons and uncover the molecular logic guiding their loading. Using APEX2-mediated proximity labeling, we identify the external transcriptome of RAB7A-positive endosomes and find a specific population of mRNAs enriched for endosomal, axonal, and synaptic functions. We find that mRNAs enriched in RAB7A endosomes contain evolutionarily conserved 5′UTRs that act as localization signals, and that the RNA-binding protein GEMIN5 interacts with these regions to promote endosomal RNA recruitment. Finally, we show that there is a conspicuous loss of endosome-associated transcripts in amyotrophic lateral sclerosis-associated conditions, accompanied by the mislocalization of GEMIN5 from endosomes. These findings uncover fundamental principles of RNA compartmentalization and highlight endosomal mRNA loading as a vulnerable axis in neuronal homeostasis.

INTRODUCTION

The endosomal organelles are dynamic membrane-bound compartments that control the movement of cargos from the plasma membrane to lysosomes for degradation or back to the cell surface for recycling.[1–3] However, recent evidence has revealed that endosomes have a crucial role as mobile platforms for the transport of RNA-protein complexes in neurons. In particular, late endosomes can carry mRNAs on their cytosolic surface, enabling localized translation and targeted protein delivery within axons and dendrites.[4–6] Despite this emerging paradigm, the molecular mechanisms governing RNA recruitment to late endosomes remain poorly understood.

Disruptions in endosomal function and defects in axonal transport are well-established hallmarks of neurodegenerative diseases, including amyotrophic lateral sclerosis (ALS),[7] where impaired vesicle trafficking contributes to neuronal dysfunction.[8–10] If RNAs fail to localize to endosomal carriers, local protein synthesis at distal sites such as synapses or mitochondria may be compromised, exacerbating neurodegeneration.[11,12]

One RNA-binding protein (RBP) of particular interest in this context is FUS, a multifunctional RBP involved in transcription, splicing, RNA transport, and translation.[13,14] Importantly, FUS also participates in vesicle-mediated RNA trafficking.[5] Several ALS-causing mutations in FUS, such as P525L, determine its cytoplasmic mis-localization and aggregation,[15] disrupt the distribution of RBPs like SMN and FMRP, also involved in RNA transport,[16,17] and impair organelle mobility in axons.[18] Given its ability to bind both RNAs and RBPs and alter their subcellular localization,[19] mutant FUS could affect RNA loading onto late endosomes, with potential consequences for local translation and neuronal homeostasis. Understanding the composition of the RNA population associated with late endosomes, the intrinsic features that drive their localization, and how disease-associated mutations affect this process is therefore crucial.

In this study, we investigate the external transcriptome of late endosomes in motor neurons (MN), define some of the molecular features that promote RNA recruitment to these vesicles, and assess the impact of the ALS-linked FUS P525L mutation on the RNA composition of this compartment. To address these questions, we applied APEX2-mediated proximity labeling[20,21] in human iPSC-derived MN, enabling selective biotinylation and purification of RNAs residing on the cytosolic surface of late endosomes. This approach allowed us to generate the first

This is an open access article under the CC BY-NC license (http://creativecommons.org/licenses/by-nc/4.0/).

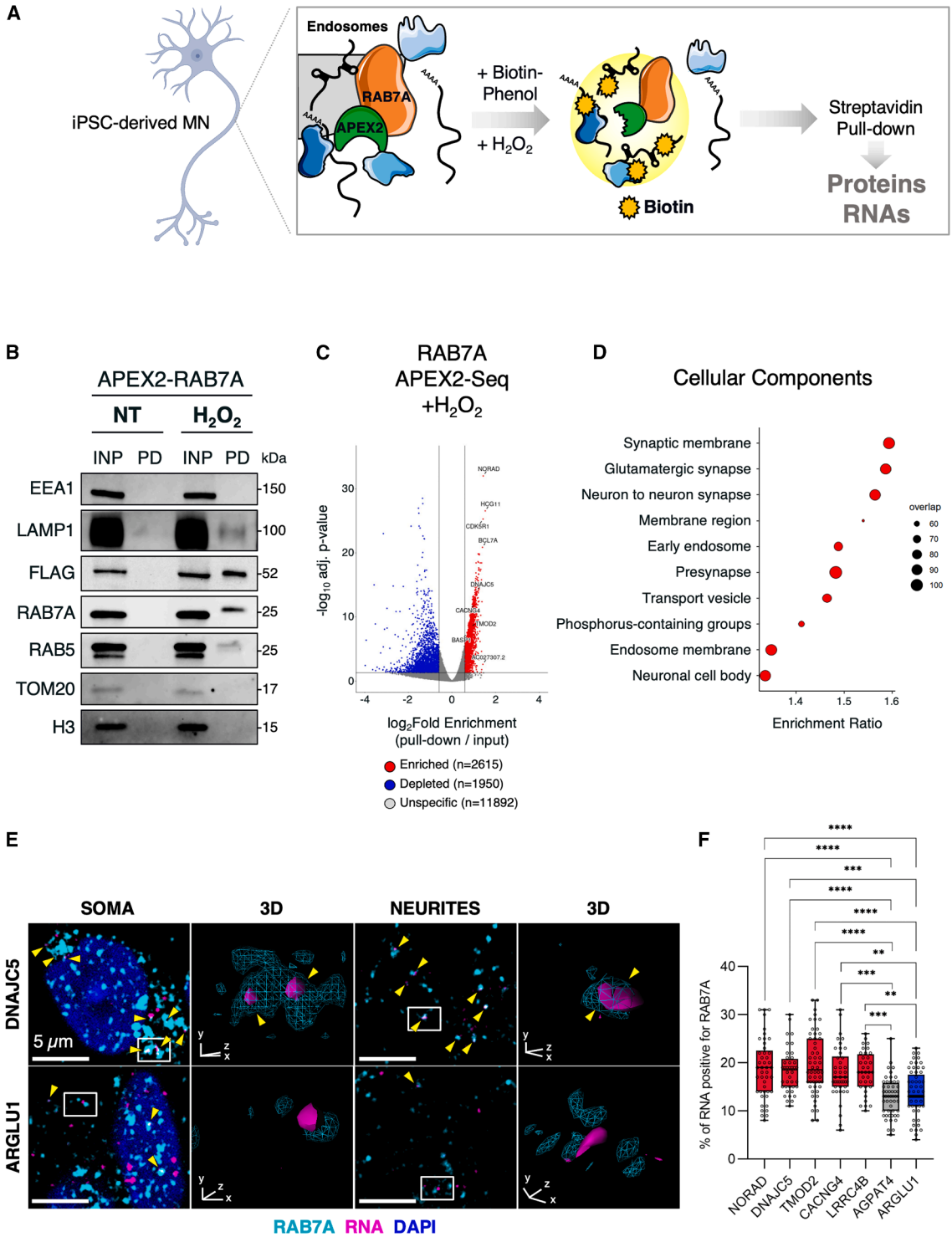


Figure 1. Proximity labeling reveals a distinct transcriptome associated with RAB7A-positive endosomes in motor neurons

(A) Schematic representation of the APEX2-based proximity labeling strategy used to biotinylate RNAs in the vicinity of RAB7A-positive endosomes in iPSC-derived MN.

(B) Western blot analysis of the APEX2-pulldown on iPSC-derived MN expressing flagged APEX2-RAB7A protein. Early endosomal markers (EEA1, RAB5), late endosomal marker (RAB7A), late endosomal/lysosomal marker (LAMP1), APEX2-RAB7A construct (FLAG), nuclear marker (H3), and mitochondrial marker (TOM20) were used to assess compartment purification. INP = 2.5% input, PD = pulldown, H_2O_2 = hydrogen peroxide treatment.

(legend continued on next page)

comprehensive map of the late endosomal external transcriptome, revealing that neuronal late endosomes selectively associate mostly with mRNAs enriched in synaptic and endosomal functions, characterized by 5′UTRs bearing localization elements. We also identify GEMIN5 as one of the RBPs involved in targeting RNA to late endosomes. Strikingly, in FUS^{P525L} MN, we observed a dramatic loss of endosome-associated RNAs, a reduction in GEMIN5 recruitment to late endosomes, and a high binding affinity of mutant FUS for endosomal RNAs, indicating that this mutant FUS disrupts endosomal RNA localization through both direct RNA binding and indirect interference with key RBPs.

Collectively, this work uncovers core principles governing RNA recruitment to late endosomes and reveals a previously unrecognized mechanism by which ALS-linked FUS mutations impair localized RNA transport, providing new insight into neurodegenerative disease pathogenesis.

RESULTS

The external transcriptome associated with RAB7A endosomes

The APEX2 proximity-labeling strategy enables biotinylation of proteins and RNAs within ~20 nm of the fusion peptide after a brief hydrogen peroxide pulse.[22] Subsequent streptavidin pulldown allows selective isolation and characterization of biotinylated molecules. We applied this approach to isolate and sequence RNAs associated with the external surface of RAB7A-positive endosomes in human iPSC-derived MN (Figure 1A); specifically, iPSCs were engineered to stably express an APEX2-RAB7A construct with a N-terminal FLAG tag and differentiated into MN.[23] Immunofluorescence allowed us to confirm that the exogenous APEX2-RAB7A peptide co-localizes with both endogenous RAB7A-positive foci (Figure S1A) and the endosomal marker CD63 (Figure S1B), and to prove that the overall number and distribution of endosomes in soma and neurites were comparable to control cells (Figure S1C). Moreover, western blot showed that exogenous APEX2-RAB7A expression levels are comparable to the endogenous RAB7A (Figure S1D). Analysis of the biotinylated proteins purified from APEX2-RAB7A MN confirmed the correct compartment targeting: along with the expected recovery of FLAG-APEX2-RAB7A protein, the endogenous late endosomal constituent RAB7A was well represented; conversely, the late endosomal-lysosomal marker LAMP1 was detected at a minor extent, while the early endosomal proteins EEA1 and RAB5 were at most barely detectable (Figure 1B). As further controls, nuclear histone H3 and mitochondrial TOM20 markers were absent in pulldown samples (Figure 1B). Notably, none of these proteins were detected in control cells not treated with hydrogen peroxide ("NT," Figure 1B). We performed RNA sequencing of pulldown-recovered RNAs and their corresponding whole-cell extracts ("input"), and we evaluated the endosomal enrichment of transcripts by comparing pulldown versus input samples. Among the 16457 RNAs expressed in MN (>1 FPKM in the input), we defined three groups: 2615 RNAs were enriched in the APEX2-RAB7A pulldown fraction (defined as "*enriched*"; $\log_2$ fold enrichment >0.59, adjusted $p < 0.05$), 1950 species resulted depleted ("*depleted*"; $\log_2$ fold enrichment < -0.59, adjusted $p < 0.05$), and 11892 were present at comparable levels in pulldown and input samples ("*unspecific*," Figure 1C). The extremely low number (5 species) of *enriched* RNAs detected in the untreated (NT) sample (Figure S1E; Table S1) demonstrated the specificity of the purification and the low background of the utilized approach. Notably, most of the endosomal "enriched" RNAs were protein coding (93.4%, Figure S1F), with specific over-representation of Gene Ontology (GO) categories related to synapses and endosomal membrane organization (Figure 1D; Figure S1G; Table S1). Moreover, KEGG pathway analysis further showed enrichment of genes involved in endocytosis and axonal development (Figure S2A; Table S1). The abundance of RAB7A-positive particles in MN neurites, detected by immunofluorescence analysis (Figure S1C), is coherent with the notion that several mRNAs encoding synaptic and endosomal proteins associate with endosomal membranes. To assess whether endosome-associated RNAs are linked to neuronal subcellular transcriptomes, we compared our dataset with published axonal[24–26] and synaptic RNA datasets.[27,28] This analysis revealed a significant enrichment of axon- and synapse-localized transcripts among endosome-associated RNAs (Figure S2B). Altogether, these results are consistent with the concept that endosomes may act as platforms for the transport and localized translation of neurite-associated mRNAs.[4]

To validate the RNA-sequencing results, we performed *in situ* RNA FISH analysis to assess the co-localization of selected endosomal-*enriched* transcripts (NORAD, DNAJC5, TMOD2, CACNG4, and LRRC4B) with endogenous RAB7A. AGPAT4 and ARGLU1 mRNAs were used as *unspecific* and *depleted* controls, respectively (Figures 1E, 1F, S3A, and S3B). Notably, all endosomal-*enriched* RNAs showed significantly higher association with RAB7A-positive particles compared to the controls. Finally, additional FISH analyses performed using either the endosomal

(C) Volcano plot showing the log2FC pulldown/input and the −log10*p*value for each RNA detected. *Enriched* and *depleted* RNAs (Padj <0.05, |log2FC| > 0.59) or *unspecific* RNAs are indicated by red, blue, and gray dots, respectively. Labels of top enriched and experimentally validated genes were reported in the plot.
(D) Dot plot depicting the cellular component GO over-represented categories of the *enriched* RNAs. Only significant categories (FDR <0.05) were depicted. The *x* axis represents category enrichment score, while *y* axis reports the GO category description. Dot size represents the number of RNAs in the analyzed group that overlap the category.
(E) Representative RNA FISH and immunofluorescence images showing localization of an endosome-*enriched* (DNAJC5) or endosome-*depleted* (ARGLU1) mRNA (magenta) relative to RAB7A-positive endosomes (cyan) in soma and neurites. Insets show 3D renderings of boxed regions. Scale bars = 5 μm. Colocalization is indicated by yellow arrows.
(F) Quantification of the percentage of endosome-*enriched* (red), *unspecific* (gray), or *depleted* (blue) RNAs associated with RAB7A-positive particles. Data are presented as Tukey's boxplots (box: median ± quartile 1–3 range; whiskers: 1.5× interquartile range). *p*-values are indicated with asterisks (**$p < 0.01$, ***$p < 0.001$, ****$p < 0.0001$). Statistical significance was assessed with one-way Brown-Forsythe and Welch ANOVA tests. $N = 3$ biological replicates (total cells: NORAD $n = 315$, DNAJC5 $n = 270$, TMOD2 $n = 278$, CACNG4 $n = 272$, LRRC4B $n = 295$, AGPAT4 $n = 269$, ARGLU1 $n = 274$).

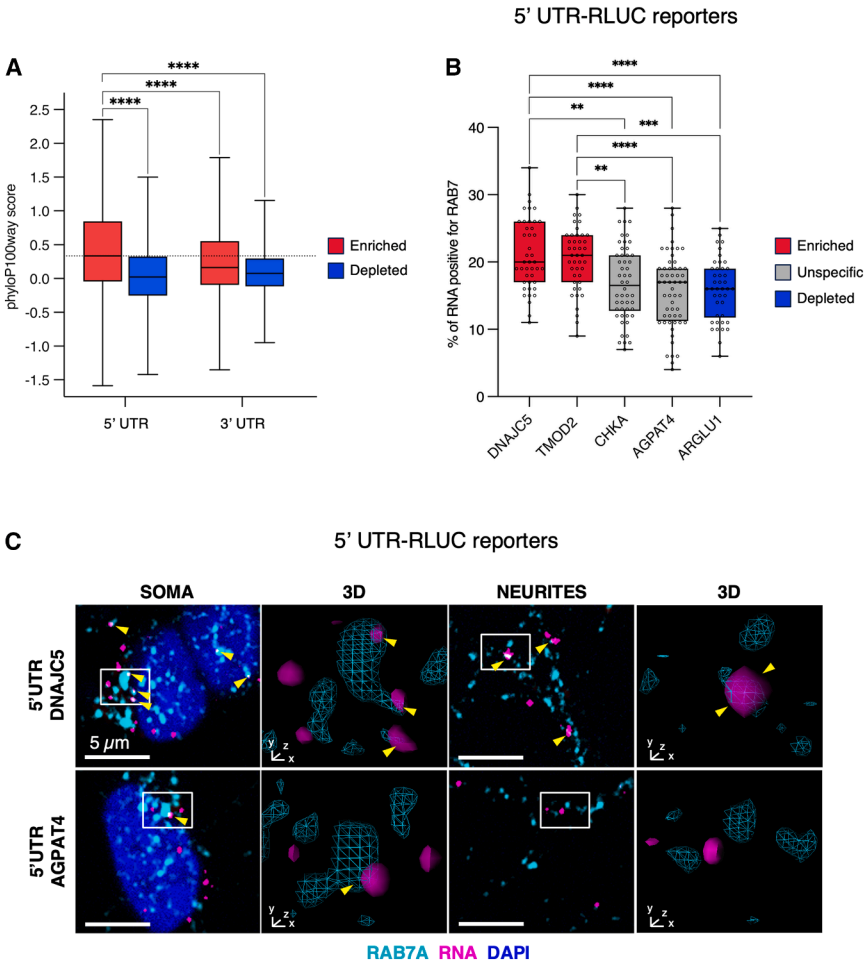


Figure 2. Conserved 5′UTR elements are sufficient to target RNAs to RAB7A-positive endosomes

(A) Distribution of PhyloP100 conservation scores for untranslated regions (UTRs). Boxplots show PhyloP100 scores for enriched (red) and depleted (blue) elements in the 5′UTR (left pair) and 3′UTR (right pair). Data are presented as Tukey's boxplots (box: median ± quartile 1–3 range; whiskers: 1.5× interquartile range). *p*-values are indicated with asterisks (****$p < 0.0001$).

(B) Quantification of the fraction of RLUC reporter mRNAs associated with RAB7A-positive endosomes when fused to 5′UTRs derived from endosome-*enriched* (red), *unspecific* (gray), or *depleted* (blue) transcripts. Data are presented as Tukey's boxplots (box: median ± quartile 1–3 range; whiskers: 1.5× interquartile range). *p*-values are indicated with asterisks (**$p < 0.01$, ***$p < 0.001$, ****$p < 0.0001$). Statistical significance was assessed with one-way Brown-Forsythe and Welch ANOVA tests. $N = 3$ biological replicates (total cells: DNAJC5 $n = 338$, TMOD2 $n = 354$, CHKA $n = 275$, AGPAT4 $n = 300$, ARGLU1 $n = 301$).

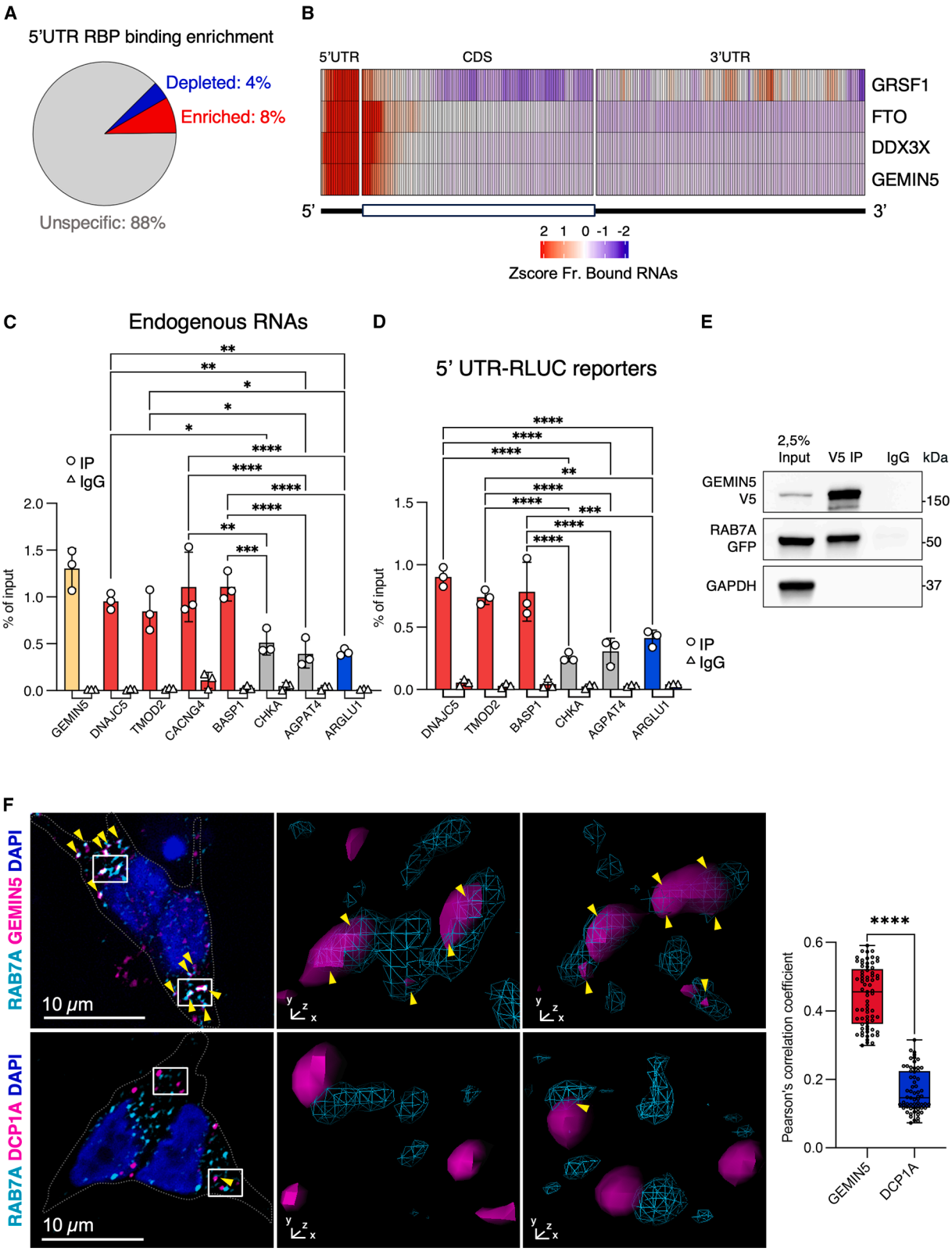
(C) Representative RNA FISH and immunofluorescence images showing localization of RLUC reporter mRNAs (magenta) fused to an endosome-*enriched* (DNAJC5) or *unspecific* (AGPAT4) 5′UTR relative to RAB7A-positive endosomes (cyan) in soma and neurites. 3D rendering of selected white boxes showing RAB7A-particles (cyan) and reporter mRNA (magenta). Scale bars = 5 μm. Colocalization is indicated by yellow arrows.

marker CD63 or the control lysosomal marker LAMP1 corroborate the specificity of the identified endosomal transcriptome (Figures S3C and S3D).

Collectively, these data demonstrate that late endosomes are enriched in MN neurites, and that their external surfaces are decorated mainly by mRNAs encoding proteins involved in synaptic and endosomal functions, consistently with their role as hubs of mRNA localization and trafficking in neurons.

5′UTR sequences are sufficient to drive RNA localization to RAB7A endosomes

The data presented above indicate that a broad population of mRNAs is specifically associated with the external surface of late endosomes. This prompted us to investigate whether intrinsic features of these transcripts could mediate their selective recruitment to the appropriate subcellular compartment. To identify RNA features driving transcript localization to endosomal membranes, we examined evolutionary conservation across 100 vertebrate species through phyloP scores and found that the 5′UTRs of *enriched* RNAs are significantly more conserved than those of *depleted* transcripts (Figure 2A). In contrast, the corresponding 3′UTRs of both groups showed a lower degree of conservation (Figure 2A), suggesting a possible role for the 5′UTR in targeting RNAs to endosomal membranes. To test whether the 5′UTR regions of *enriched* RNAs are sufficient to mediate endosome association, we generated



(legend on next page)

iPSC-derived MN stably expressing luciferase reporter constructs. The *Renilla* Luciferase ORF was fused to different 5′UTRs selected either among the endosome-*enriched* transcripts (DNAJC5 and TMOD2) or among different controls (CHKA-*unspecific*, AGPAT4-*unspecific* and ARGLU1-*depleted*). Co-localization between the reporter mRNAs and RAB7A was then assessed by immunofluorescence combined with RNA FISH. The data show that reporter RNAs carrying the 5′UTRs of endosome-*enriched* transcripts displayed significantly higher overlap with RAB7A-positive particles compared to those bearing control 5′UTRs (Figure 2B). Examples of FISH analysis for couples of *enriched* versus *depleted* RNAs with similar expression levels (Figure S4A) are shown in Figures 2C and S4B. Altogether, this evidence suggests that the 5′UTRs of endosomal-*enriched* RNAs are sufficient to drive endosomal RNA localization.

GEMIN5 binds the 5′UTR of endosome-associated mRNAs

RNA localization can be achieved through the interaction with specific RBPs, which are able to recognize binding sites usually located within the UTR sequences of RNAs.[29–31] In order to identify RBPs possibly involved in the localization to endosomes, we analyzed the ENCODE eCLIP compendium[32] focusing on the subgroup of factors with predominant cytoplasmic localization (49 RBPs; see Methods). We identified four RBPs that preferentially bind the 5′ UTRs of endosome-*enriched* transcripts compared to *depleted* ones (FDR < 0.05, log2 OR > 0; Figure 3A; Table S2). Notably, the four RBPs showed a preferential and specific binding within the 5′UTRs of *enriched* transcripts rather than in other regions (Figure 3B). Among the four candidates (GEMIN5, FTO, DDX3X, and GRSF1), we selected GEMIN5 as the most promising factor for potential involvement in recruiting and transporting RNA to endosomal membranes. Indeed, unlike the ubiquitously distributed demethylase FTO, the broadly expressed helicase DDX3X, or the mitochondria-enriched RBP GRSF1, GEMIN5 is known to form cytoplasmic RNA granules and to function as a selective mRNA-carrying RNP hub in neurons, exhibiting dynamics that closely mirror those of endosome-associated mRNAs.[33] However, we do not exclude that the other candidates may also contribute to endosomal RNA localization. To assess whether GEMIN5 directly binds endosomal-*enriched* RNAs, we generated SK-N-BE neuroblastoma cell lines stably expressing a V5-tagged version of GEMIN5. The immunoprecipitation of GEMIN5-V5 upon UV crosslinking revealed a preferential binding of the protein to the endosomal-*enriched* transcripts (DNAJC5, TMOD2, BASP1, and CACNG4; Figure 3C; Figures S5A and S5B), with enrichment comparable to the IP positive control (GEMIN5 own mRNA[34]) and significantly higher than that of non-endosomal RNAs (CHKA, AGPAT4, and ARGLU1). To further assess the specificity of GEMIN5 binding to the 5′UTRs of endosome-enriched RNAs, we generated SK-N-BE cells co-expressing GEMIN5-V5 together with individual 5′UTR-RLUC reporter constructs that are expressed at comparable levels (Figure S5C). CLIP analysis in these cells (Figure S5D) demonstrated that GEMIN5 binds the 5′UTR-RLUC transcripts derived from endosome-enriched RNAs in a significantly higher manner with respect to control reporters (Figure 3D). Notably, the efficiency of IP was comparable among the experiments (Figures S5A, S5B, and S5D). Consistently, co-immunoprecipitation (Figure 3E) and immunofluorescence in MN (Figure 3F) confirmed the interaction between GEMIN5 and RAB7A. Moreover, GEMIN5 displays a higher and statistically significant level of co-localization with RAB7A than the negative control DCP1A, a marker of cytoplasmic P-bodies (Figure 3F; Figure S5E). Taken together, these results indicate that GEMIN5 localizes to late endosomes, specifically binds endosomal-*enriched* RNAs through their 5′UTRs, and may act as a driver of RNA localization onto these vesicles.

GEMIN5 localizes mRNAs to RAB7A endosomes through binding to their 5′UTR

To determine whether GEMIN5 plays a functional role in regulating endosomal RNA localization, we performed its down-regulation through RNA interference in SK-N-BE cells (Figure S6A) and analyzed the localization of its RNA interactors using immunofluorescence for RAB7A combined with RNA FISH. We examined two endosome-*enriched* GEMIN5 RNA interactors (DNAJC5 and TMOD2; see Figures 1F and 3C), together with two control RNAs that neither associate with endosomes nor interact with GEMIN5 (ARGLU1, *depleted*, and

Figure 3. GEMIN5 binds the 5′UTR of endosome-*enriched* RNAs and localizes on late endosomes

(A) Pie chart showing the fraction of enriched, depleted, or unspecific RBPs among 49 cytoplasmic RBPs from the ENCODE eCLIP compendium, as determined by RBP binding enrichment analysis on the 5′UTRs of RNAs enriched or depleted in endosomes.

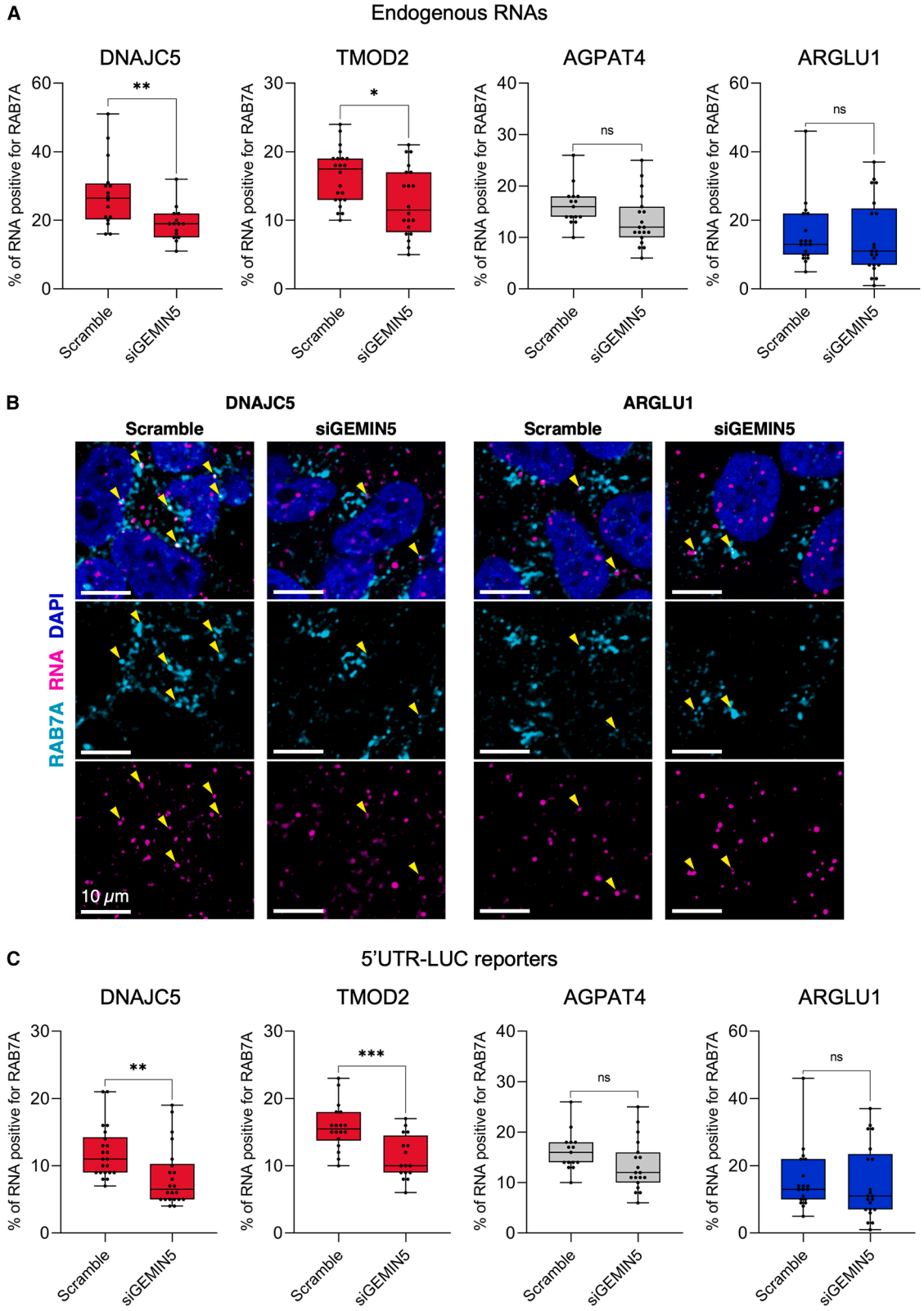
(B) Meta-transcript heatmap showing the z-scored fraction of bound endosomal RNAs across transcript regions (5′UTR, CDS, and 3′UTR) for the indicated RBPs (GRSF1, FTO, DDX3X, and GEMIN5). Color indicates relative enrichment (red) or depletion (blue) along the 5′–3′ axis.

(C) qPCR quantification of endogenous endosome-*enriched* (red), *unspecific* (gray), and *depleted* (blue) RNAs recovered by GEMIN5-V5 immunoprecipitation in SK-N-BE cells, expressed as percentage of input. GEMIN5 mRNA serves as a positive control (yellow). Data are presented as mean ± SD ($N = 3$). p-values are indicated with asterisks (*$p < 0.05$, **$p < 0.01$, ***$p < 0.001$, ****$p < 0.0001$). Statistical significance was assessed with one-way ANOVA with Tukey multiple comparisons test.

(D) qPCR quantification of RLUC reporter mRNAs fused to 5′UTRs from endosome-*enriched* (red), *unspecific* (gray), or *depleted* (blue) transcripts recovered by GEMIN5-V5 immunoprecipitation in SK-N-BE cells, expressed as percentage of input. Data are presented as mean ± SD ($N = 3$). p-values are indicated with asterisks (*$p < 0.05$, **$p < 0.01$, ***$p < 0.001$, ****$p < 0.0001$). Statistical significance was assessed with one-way ANOVA with Tukey multiple comparisons test.

(E) Co-immunoprecipitation showing interaction between GEMIN5-V5 and RAB7A-GFP in neuroblastoma cells; GAPDH serves as a negative control.

(F) Left, immunofluorescence analysis of GEMIN5 or the P-bodies marker DCP1A (magenta) relative to RAB7A-positive endosomes (cyan). Insets show 3D renderings of boxed regions. Scale bars = 10 μm. Right, quantification of colocalization by Pearson's correlation coefficient. Data are presented as Tukey's boxplots (box: median ± quartile 1–3 range; whiskers: 1.5× interquartile range). p-value is indicated with asterisks (****$p < 0.0001$). Statistical significance was assessed with two-tailed, unpaired t test. $N = 3$ biological replicates (total cells: GEMIN5 $n = 323$, DCP1A = 259).



(legend on next page)

AGPAT4, *unspecific*; see Figures 1F and 3C). Quantification of RNA spots colocalizing with RAB7A showed that GEMIN5 depletion significantly impaired the endosomal localization of *enriched* RNAs, whereas control transcripts remained unaffected (Figure 4A; Figure 4B). Consistently, the same experiment using the corresponding 5′UTR-RLUC reporters yielded similar results: DNAJC5 and TMOD2 constructs showed reduced endosomal colocalization upon GEMIN5 knockdown, while the AGPAT4 and ARGLU1 controls were unaffected (Figures 4C; Figures S6B and S6C). Taken together, these data demonstrate that GEMIN5 is required for proper endosomal localization of *enriched* RNAs that harbor a 5′UTR capable of interacting with this protein.

The ALS-associated mutant FUS^{P525L} impairs RNA recruitment to RAB7A endosomes

Recently, disruption of vesicular trafficking has clearly emerged as a hallmark of multiple neurodegenerative diseases, including ALS.[9,35,36] In particular, ALS-associated mutants of FUS protein, which mislocalize to the cytoplasm where they promote aggregate formation, have been shown to sequester key RBPs involved in RNA transport, such as IMP1,[37] SMN,[16] and Kinesin1.[38] Therefore, we investigated the impact of the ALS-linked FUS^{P525L} mutation on the composition of the endosomal transcriptome. To assess whether this mutation alters the endosomal transcriptome, we performed APEX2-RAB7A-seq in isogenic iPSC-derived MN homozygous for FUS^{P525L}. Efficient and specific biotinylation of endosomal proteins was confirmed by streptavidin-based pulldown followed by western blotting (Figure S7A). Strikingly, RNA-seq analysis revealed a major collapse of the endosomal transcriptome. Of the 17,760 RNAs expressed (>1 FPKM in input), only 329 were enriched in FUS^{P525L} MN, compared to 2,615 in control cells (Figure 5A). In addition, 662 were depleted, and 16,768 remained unchanged (Figure S7B; Table S1), with no *enriched* RNAs in the untreated (NT) samples (Figure S7C). Thus, approximately 91% of RNAs normally enriched at late endosomes in wild-type MN were depleted in the FUS^{P525L} background, indicating a profound defect in endosomal RNA recruitment. To validate these findings, we performed immunofluorescence coupled with RNA FISH for transcripts that were selectively lost from endosomes in FUS^{P525L} conditions. As shown in Figures 5B and C, CACNG4 and TMOD2 RNAs, classified in the "*loss*" fraction by our sequencing analysis, exhibited a significant reduction in the association with RAB7A-positive endosomes. Representative examples for CACNG4 and TMOD2 mRNAs are shown in Figures 5 and S7D, respectively. By contrast, NORAD, belonging to the "*common*" group, and AGPAT4, excluded from endosomes in both conditions, maintained their localization even in FUS^{P525L} cells (Figure 5B). To give functional insights into these observations, we investigated the neuritic distribution of a "loss" (CACNG4) and a control (AGPAT4) RNA in wild-type and FUS^{P525L} MN, demonstrating that the impaired association with RAB7A endosomes in the FUS-mutated context results in a reduced neuritic localization (Figures 5D and E).

Taken together, these results reveal a profound collapse of the endosomal transcriptome in ALS-associated conditions, with implications for RNA trafficking in neurites.

The ALS-associated mutant FUS^{P525L} prevents the localization of GEMIN5-RNA complexes to RAB7A endosomes

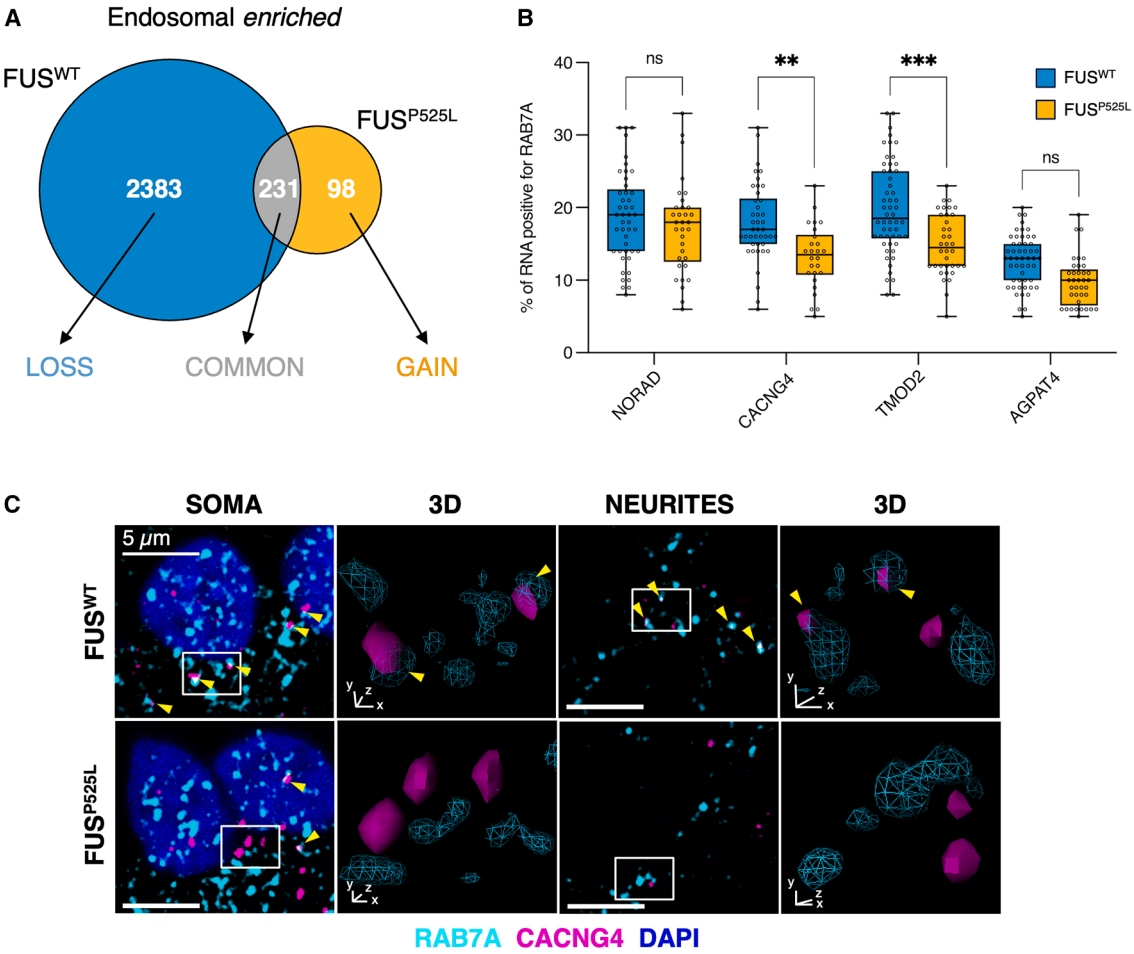
Given the role of GEMIN5 in promoting endosomal RNA localization, we next asked whether its recruitment to late endosomes was impaired in the presence of FUS^{P525L}. Immunofluorescence analysis revealed a significant reduction in the colocalization between GEMIN5 and RAB7A, as quantified by Pearson's correlation coefficient (Figures S8A and S8B). This observation is further confirmed by Proximity Ligation Assay (PLA) (Figure 6A), showing that GEMIN5-RAB7A PLA spot density significantly decreases in the FUS mutant context. Notably, GEMIN5 CLIP experiments showed that the interaction of GEMIN5 with CACNG4 and TMOD2 was not affected in FUS^{P525L} cells (Figure S8C), indicating that the exclusion of these RNAs from endosomes is not due to a failure in GEMIN5 binding. Interestingly, we also found that FUS interacts with GEMIN5, as demonstrated by both PLA and reciprocal co-immunoprecipitation (Figures 6B–D), and that this interaction is significantly higher in the FUS mutant context (Figure 6B). Altogether, these findings support a model in which mutant FUS sequesters GEMIN5, leading to defects in localization to endosomes for a specific class of transcripts. Since FUS can also directly bind RNA, we tested whether it could subtract endosomal-*enriched* transcripts through direct binding. Therefore, we interrogated previously published PAR-CLIP data for FUS^{P525L} generated in human iPSC-derived MN[39] to assess its binding propensity toward endosomal RNAs. Interestingly, we found that FUS^{P525L} has high binding propensity for endosomal RNAs and that 48% of the 822 RNAs with the highest affinity for FUS (top 10% based on the proportion of PAR-CLIP transitions) are depleted from endosomes in the mutant context (Figure S8D). CLIP analysis for FUS further confirmed the interaction with TMOD2 and CACNG4 as representative of the loss fraction (Figure S8E). Notably,

Figure 4. GEMIN5 is required for 5′UTR-dependent RNA recruitment to RAB7A-positive endosomes

(A) Quantification of endogenous RNA association with RAB7A-positive endosomes in control (Scramble) and GEMIN5 knockdown (siGEMIN5) SK-N-BE cells. Endosome-*enriched* (red), *unspecific* (gray), and *depleted* (blue) transcripts are shown. Data are presented as Tukey's boxplots (box: median ± quartile 1–3 range; whiskers: 1.5× interquartile range). *p*-values are indicated with asterisks (*$p < 0.05$, **$p < 0.01$). Statistical significance was assessed with two-tailed, unpaired *t* test. $N = 3$ biological replicates.

(B) Representative RNA FISH and immunofluorescence images showing localization of an endosome-*enriched* (DNAJC5) or endosome-*depleted* (ARGLU1) mRNA (magenta) relative to RAB7A-positive endosomes (cyan) in control (Scramble) and GEMIN5 knockdown (siGEMIN5) SK-N-BE cells. Scale bars = 10 μm. Colocalization is indicated by yellow arrows.

(C) Quantification of RAB7A association for RLUC reporter mRNAs fused to 5′UTRs from endosome-*enriched* (red), *unspecific* (gray), or *depleted* (blue) transcripts in control and GEMIN5 KD conditions. Data are presented as Tukey's boxplots (box: median ± quartile 1–3 range; whiskers: 1.5× interquartile range). *p*-values are indicated with asterisks (**$p < 0.01$, ***$p < 0.001$). Statistical significance was assessed with two-tailed, unpaired *t* test. $N = 3$ biological replicates.



(legend on next page)

immunofluorescence analysis revealed no significant alteration in the number of RAB7A-positive particles in FUS^{P525L} MN (Figure S8F).

Consequently, the concomitant displacement of GEMIN5, FUS, and their RNA targets from RAB7A-positive endosomes indicates that FUS^{P525L} disrupts RNA recruitment to endosomes via both direct and indirect mechanisms.

DISCUSSION

By defining the external transcriptome of RAB7A-positive late endosomes in human iPSC-derived MN, we reveal that these vesicles are associated with mRNAs encoding endosomal, axonal, and synaptic regulators. These data, together with the notion that many of these transcripts are known to be localized at the neuronal periphery,[26] support a direct role for endosomes as platforms for mRNA trafficking and, possibly, local translation in neurites. This extends previous observations that endolysosomal vesicles transport mRNA–protein complexes in neurons,[4,40] establishing a molecular framework for RNA recruitment to this compartment.

Mechanistically, we identify the 5′UTR of the mRNAs associated with APEX2-RAB7A endosomes as a key element governing RNA localization. These regions alone are sufficient to direct mRNAs to late endosomes and, for a specific subclass of transcripts, we found that the RBP GEMIN5 mediates endosomal loading. GEMIN5 is a core component of the SMN complex, which has been implicated in RNA transport[33] and neuronal ribonucleoprotein granule dynamics; other evidence describes the ability of this protein in regulating several aspects of RNA metabolism through a complex network of interactors.[34,41] Our data position it as a previously unrecognized mediator linking endosomal vesicles to selective RNA cargo. This expands the functional repertoire of GEMIN5 beyond its canonical roles in snRNP assembly and axonal RNA granules, suggesting that neurons may utilize shared RNA-binding factors to coordinate distinct localization pathways converging on translation-competent organelles. However, we cannot exclude that GEMIN5 acts in cooperation with other factors to drive this localization, like DDX3X, FTO, and GRSF1, which were also highlighted by our bioinformatic predictions. Moreover, contrary to prevailing models that emphasize 3′UTRs as the primary drivers of mRNA localization,[42] our data highlight a major role for the 5′UTRs in mediating mRNA targeting to endosomal membranes. Strikingly, we find that the ALS-associated FUS^{P525L} mutation profoundly disrupts the endosomal RNA landscape; nearly all RNAs normally enriched at endosomes in wild-type neurons are lost in cells expressing mutant FUS. This collapse of the endosomal transcriptome coincides with reduced GEMIN5 association with endosomes. This, together with the finding that FUS interacts with GEMIN5, is consistent with a model in which the cytoplasmic mutant FUS sequesters GEMIN5 away from late endosomal membranes. Moreover, the ability of mutant FUS to directly bind a relevant subset of endosomal RNAs suggests a possible additional mechanism of interference, involving competition with GEMIN5 (and other hypothetical interactors) for RNA binding. These findings, together with the reduced neuritic localization of specific endosome-associated RNAs in the FUS mutant context, provide a molecular link between ALS-linked defects in RNA transport, organelle dynamics, and localized translation, and suggest that impaired endosomal RNA loading may contribute to synaptic and axonal dysfunction in the disease.

Together, our data establish a previously unrecognized mechanism for mRNA localization to late endosomes in neurons and reveal its vulnerability to ALS-associated perturbations. By defining the *cis*-acting features and *trans*-acting factors that govern RNA loading onto endosomal membranes, we provide a framework to understand how transcriptomic compartmentalization supports neuronal homeostasis.

Limitations of the study

Although this study offers novel insights into the subcellular distribution of RNA in MN and its alteration in ALS conditions, some limitations should be considered. First, our APEX2-based proximity labeling approach relies on PiggyBac transposon-mediated generation of stable cell lines. Even though APEX2-RAB7A is expressed at near-physiological levels and does not alter the abundance or distribution of RAB7-positive endosomes, this strategy is unlikely to label the entire endosomal population. This partial labeling may contribute to the moderate enrichment observed for endosome-associated transcripts. Second, our mechanistic investigation focused primarily on

Figure 5. ALS-related FUS^{P525L} mutation disrupts endosomal RNA recruitment

(A) Venn diagram showing the overlap between endosome-*enriched* RNAs identified in FUS^{WT} and FUS^{P525L} iPSCs-derived MN.

(B) Quantification of RAB7A association for representative RNAs that are commonly enriched (NORAD), selectively lost in FUS^{P525L} neurons (CACNG4, TMOD2), or commonly excluded (AGPAT4). Data are presented as Tukey's boxplots (box: median ± quartile 1–3 range; whiskers: 1.5× interquartile range). *p*-values are indicated with asterisks (*$p < 0.05$, **$p < 0.01$, ***$p < 0.001$). Statistical significance was assessed with a two-way ANOVA with Šidak's multiple comparison test. $N = 3$ biological replicates (total cells: FUS^{WT} NORAD $n = 315$, CACNG4 $n = 272$, TMOD2 $n = 278$, AGPAT4 $n = 269$; FUS^{P525L} NORAD $n = 349$, CACNG4 $n = 257$, TMOD2 $n = 282$, AGPAT4 $n = 260$).

(C) Representative RNA FISH and immunofluorescence images showing CACNG4 mRNA (magenta) relative to RAB7A-positive endosomes (cyan) in soma and neurites, in FUS^{WT} and FUS^{P525L} MN. Scale bars = 5 μm. Colocalization is indicated by yellow arrows. 3D rendering of selected white boxes showing RAB7A-particles (cyan) and CACNG4 mRNA (magenta).

(D) Left: representative images showing β-III tubulin (TUBBIII, red) and CACNG4 RNA (gray, selectively lost in FUS^{P525L}) in FUS^{WT} and FUS^{P525L} MN. Scale bars = 5 μm. RNA in neurites is indicated by yellow arrows. Right: Quantification of FISH spots normalized on cell area. Data are presented as Tukey's boxplots (box: median ± quartile 1–3 range; whiskers: 1.5× interquartile range). *p*-value is indicated with asterisks (*$p < 0.05$). Statistical significance was assessed with two-tailed, unpaired *t* test. $N = 3$ biological replicates.

(E) Left: representative images showing β-III tubulin (TUBBIII, red) and AGPAT4 RNA (gray, commonly excluded from endosomes), in FUS^{WT} and FUS^{P525L} MN. Scale bars = 5 μm. Right: Quantification of FISH spots normalized on cell area. Data are presented as Tukey's boxplots (box: median ± quartile 1–3 range; whiskers: 1.5× interquartile range). *p*-value is indicated with asterisks (*$p < 0.05$). Statistical significance was assessed with two-tailed, unpaired *t* test. $N = 3$ biological replicates.

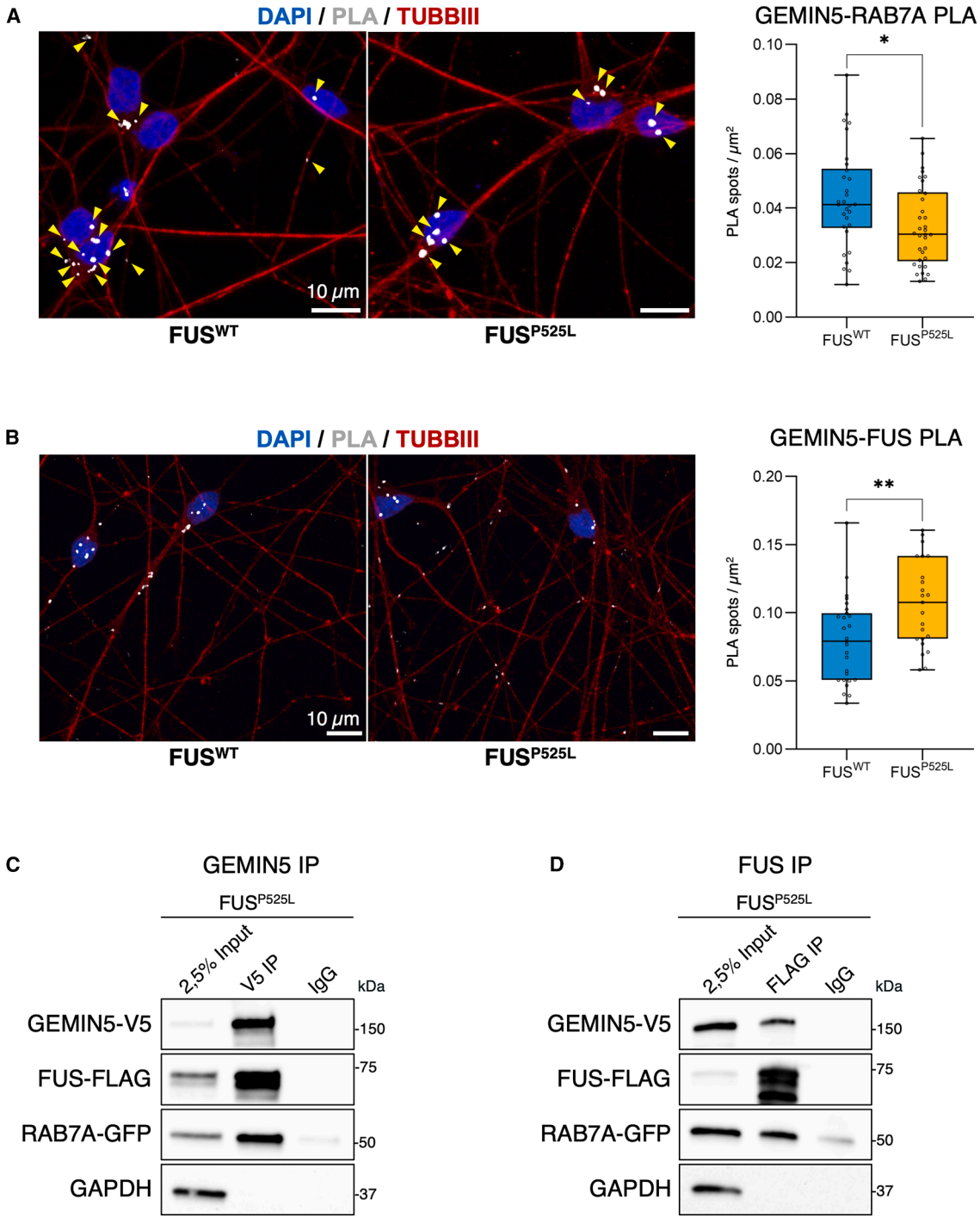


Figure 6. ALS-related FUS^{P525L} impairs GEMIN5-RNA complexes recruitment onto late endosomes

(A) Left, representative confocal max intensity z-projection images showing GEMIN5-RAB7A PLA spots (gray), β-III tubulin (TUBBIII, red), and DAPI (blue) in FUS^{WT} and FUS^{P525L} MN. PLA spots are indicated by yellow arrows. Scale bars = 10 μm. Right, quantification of PLA spot density in FUS^{WT} and FUS^{P525L} MN. Data are presented as Tukey's boxplots (box: median ± quartile 1–3 range; whiskers: 1.5× interquartile range). *p*-value is indicated with asterisks (*$p < 0.05$). Statistical significance was assessed with a two-tailed, unpaired *t* test. *N* = 3 biological replicates.

(B) Left, representative confocal max intensity z-projection images showing GEMIN5-FUS PLA spots (gray), β-III tubulin (TUBBIII, red), and DAPI (blue) in FUS^{WT} and FUS^{P525L} MN. Scale bars = 10 μm. Right, quantification of PLA spot density in FUS^{WT} and FUS^{P525L} MN. Data are presented as Tukey's boxplots (box: median ± quartile 1–3 range; whiskers: 1.5× interquartile range). *p*-value is indicated with asterisks (**$p < 0.01$). Statistical significance was assessed with a two-tailed, unpaired *t* test. *N* = 3 biological replicates.

(legend continued on next page)

GEMIN5 as a mediator of RNA recruitment to late endosomes. Our analysis of proteins with a high-binding potential for endosome-enriched RNAs identified additional RBPs that may contribute to this process, either independently or in concert with GEMIN5; however, investigating their contribution was beyond the scope of this study. Moreover, while our findings establish GEMIN5 as a key regulator of endosomal RNA localization, we did not assess the consequences of GEMIN5 depletion in MN or its impact on neuronal physiology. Addressing the functional interplay between GEMIN5 and other candidate RNA-binding proteins, as well as defining the contribution of GEMIN5 to neuronal function, will be important directions for future studies. Finally, the altered neuritic distribution of endosomal RNA caused by FUS mutation was evaluated using only a few representative transcripts. Our bioinformatic analysis demonstrates the endosomal enrichment of RNAs associated with synaptic and axonal functions, suggesting that this mechanism likely regulates a broader set of localized RNAs, the extent of which remains to be determined.

RESOURCE AVAILABILITY

Lead contact

Requests for further information and resources should be directed to and will be fulfilled by the lead contact, Irene Bozzoni (irene.bozzoni@uniroma1.it).

Materials availability

All materials generated in this study will be available upon request from the lead contact under a material transfer agreement.

Data and code availability

- The high-throughput sequencing data generated in this study have been deposited in the GEO database under accession code: GSE316825.
- The paper does not report original code; bioinformatic analysis pipelines and tools utilized in this study are described in the method details section.
- Any additional information required to reanalyze the data reported in this paper is available from the lead contact upon request.

ACKNOWLEDGMENTS

We thank M. Marchioni for technical help and M. Caruso for assistance. We thank Prof. M. Morlando and Prof. A. Rosa for discussion. This work was partially supported by grants from ERC-2019-SyG 855923-ASTRA, AIRC IG 2019 Id. 23053, and the National Center for Gene Therapy and Drug based on RNA Technology (CN00000041) and NextGenerationEU PNRR MUR to I.B., and PRIN 2022HM5LFW to J.M. We thank Prof. Alberto Diaspro and Dr. Paolo Bianchini (Nanoscopy & NIC@IIT, Istituto Italiano di Tecnologia), Dr. Michele Oneto (Nikon Imaging Center), and Marco Scotto (Molecular Microscopy and Spectroscopy, Istituto Italiano di Tecnologia) for experimental support in confocal microscopy. We are also grateful to Dr. Diego Vozzi and the Genomic Facility of IIT for support in RNA sequencing experiments.

AUTHOR CONTRIBUTIONS

I.B., D.M., A.S., and L.S.M. conceptualized the project. I.B., D.M., A.S., and J.M. supervised and coordinated the experiments. L.S.M. and D.M. set up the experimental system with the contribution of F.C. and performed molecular biology experiments. A.S. and A.D.A. designed and performed the bioinformatic analyses. L.S.M., T.S., E.V., and D.M. performed the IF and smFISH experiments and designed the analysis. L.S.M., T.S., and V.P. analyzed the imaging experiments. J.M. analyzed the results and discussed the data. I.B., D.M., A.S., and L.S.M. wrote the original manuscript with contributions from all the authors.

DECLARATION OF INTERESTS

The authors declare no competing interests.

STAR★METHODS

Detailed methods are provided in the online version of this paper and include the following:

- KEY RESOURCES TABLE
- EXPERIMENTAL MODEL AND STUDY PARTICIPANT DETAILS
  - Human cell lines
- METHOD DETAILS
  - Cell culture, maintenance and treatments
  - Cloning and stable cell lines generation
  - iPSCs differentiation into spinal motor neurons
  - RNA extraction and analysis
  - Protein extraction and analysis
  - APEX2-pulldown of proteins and RNAs
  - Library preparation and RNA-seq analysis
  - RBP binding enrichment analysis
  - Conservation analysis
  - Localization analysis
  - Immunofluorescence analysis
  - Single-molecule fluorescence *in situ* hybridization analysis
  - Proximity Ligation Assay (PLA) and analysis
  - UV-crosslinked immunoprecipitation (CLIP)
  - Co-immunoprecipitation
- QUANTIFICATION AND STATISTICAL ANALYSIS

SUPPLEMENTAL INFORMATION

Supplemental information can be found online at https://doi.org/10.1016/j.celrep.2026.118206.

Received: February 26, 2026
Revised: August 10, 2026
Accepted: October 7, 2026

REFERENCES

1. Huotari, J., and Helenius, A. (2011). Endosome maturation. EMBO J. *30*, 3481–3500. https://doi.org/10.1038/emboj.2011.286.
2. Yap, C.C., and Winckler, B. (2012). Harnessing the Power of the Endosome to Regulate Neural Development. Neuron *74*, 440–451. https://doi.org/10.1016/j.neuron.2012.04.015.
3. Cullen, P.J., and Steinberg, F. (2018). To degrade or not to degrade: mechanisms and significance of endocytic recycling. Nat. Rev. Mol. Cell Biol. *19*, 679–696. https://doi.org/10.1038/s41580-018-0053-7.
4. Cioni, J.-M., Lin, J.Q., Holtermann, A.V., Koppers, M., Jakobs, M.A.H., Azizi, A., Turner-Bridger, B., Shigeoka, T., Franze, K., Harris, W.A., and Holt, C.E. (2019). Late Endosomes Act as mRNA Translation Platforms

(C) Representative western blot of immunoprecipitation for GEMIN5-V5 showing its interaction with FLAG-FUS^{P525L} and RAB7A-GFP in SK-N-BE cells. GAPDH serves as a negative control. $N = 3$ biological replicates.
(D) Representative western blot of immunoprecipitation for FLAG-FUS^{P525L} demonstrating its interaction with GEMIN5-V5 and RAB7A-GFP. GAPDH serves as a negative control. $N = 3$ biological replicates.

and Sustain Mitochondria in Axons. Cell *176*, 56–72.e15. https://doi.org/10.1016/j.cell.2018.11.030.

5. Liao, Y.-C., Fernandopulle, M.S., Wang, G., Choi, H., Hao, L., Drerup, C.M., Patel, R., Qamar, S., Nixon-Abell, J., Shen, Y., et al. (2019). RNA Granules Hitchhike on Lysosomes for Long-Distance Transport, Using Annexin A11 as a Molecular Tether. Cell *179*, 147–164.e20. https://doi.org/10.1016/j.cell.2019.08.050.
6. Schuhmacher, J.S., tom Dieck, S., Christoforidis, S., Landerer, C., Davila Gallesio, J., Hersemann, L., Seifert, S., Schäfer, R., Giner, A., Toth-Petroczy, A., et al. (2023). The Rab5 effector FERRY links early endosomes with mRNA localization. Mol. Cell *83*, 1839–1855.e13. https://doi.org/10.1016/j.molcel.2023.05.012.
7. Burk, K., and Pasterkamp, R.J. (2019). Disrupted neuronal trafficking in amyotrophic lateral sclerosis. Acta Neuropathol. *137*, 859–877. https://doi.org/10.1007/s00401-019-01964-7.
8. Alami, N.H., Smith, R.B., Carrasco, M.A., Williams, L.A., Winborn, C.S., Han, S.S.W., Kiskinis, E., Winborn, B., Freibaum, B.D., Kanagaraj, A., et al. (2014). Axonal Transport of TDP-43 mRNA Granules Is Impaired by ALS-Causing Mutations. Neuron *81*, 536–543. https://doi.org/10.1016/j.neuron.2013.12.018.
9. Sleigh, J.N., Tosolini, A.P., Gordon, D., Devoy, A., Fratta, P., Fisher, E.M.C., Talbot, K., and Schiavo, G. (2020). Mice Carrying ALS Mutant TDP-43, but Not Mutant FUS, Display In Vivo Defects in Axonal Transport of Signaling Endosomes. Cell Rep. *30*, 3655–3662.e2. https://doi.org/10.1016/j.celrep.2020.02.078.
10. Todd, T.W., Shao, W., Zhang, Y.J., and Petrucelli, L. (2023). The endolysosomal pathway and ALS/FTD. Trends Neurosci. *46*, 1025–1041. https://doi.org/10.1016/j.tins.2023.09.004.
11. Pushpalatha, K.V., and Besse, F. (2019). Local Translation in Axons: When Membraneless RNP Granules Meet Membrane-Bound Organelles. Front. Mol. Biosci. *6*, 129. https://doi.org/10.3389/fmolb.2019.00129.
12. Piol, D., Robberechts, T., and Da Cruz, S. (2023). Lost in local translation: TDP-43 and FUS in axonal/neuromuscular junction maintenance and dysregulation in amyotrophic lateral sclerosis. Neuron *111*, 1355–1380. https://doi.org/10.1016/j.neuron.2023.02.028.
13. Ratti, A., and Buratti, E. (2016). Physiological functions and pathobiology of TDP-43 and FUS/TLS proteins. J. Neurochem. *138*, 95–111. https://doi.org/10.1111/jnc.13625.
14. Birsa, N., Bentham, M.P., and Fratta, P. (2020). Cytoplasmic functions of TDP-43 and FUS and their role in ALS. Semin. Cell Dev. Biol. *99*, 193–201. https://doi.org/10.1016/j.semcdb.2019.05.023.
15. Kwiatkowski, T.J., Bosco, D.A., LeClerc, A.L., Tamrazian, E., Vanderburg, C.R., Russ, C., Davis, A., Gilchrist, J., Kasarskis, E.J., Munsat, T., et al. (2009). Mutations in the FUS/TLS Gene on Chromosome 16 Cause Familial Amyotrophic Lateral Sclerosis. Science *323*, 1205–1208. https://doi.org/10.1126/science.1166066.
16. Groen, E.J.N., Fumoto, K., Blokhuis, A.M., Engelen-Lee, J., Zhou, Y., van den Heuvel, D.M.A., Koppers, M., van Diggelen, F., van Heest, J., Demmers, J.A.A., et al. (2013). ALS-associated mutations in FUS disrupt the axonal distribution and function of SMN. Hum. Mol. Genet. *22*, 3690–3704. https://doi.org/10.1093/hmg/ddt222.
17. Birsa, N., Ule, A.M., Garone, M.G., Tsang, B., Mattedi, F., Chong, P.A., Humphrey, J., Jarvis, S., Pisiren, M., Wilkins, O.G., et al. (2021). FUS-ALS mutants alter FMRP phase separation equilibrium and impair protein translation. Sci. Adv. *7*, eabf8660. https://doi.org/10.1126/sciadv.abf8660.
18. Guo, W., Naujock, M., Fumagalli, L., Vandoorne, T., Baatsen, P., Boon, R., Ordovás, L., Patel, A., Welters, M., Vanwelden, T., et al. (2017). HDAC6 inhibition reverses axonal transport defects in motor neurons derived from FUS-ALS patients. Nat. Commun. *8*, 861. https://doi.org/10.1038/s41467-017-00911-y.
19. Mariani, D., Setti, A., Castagnetti, F., Vitiello, E., Stufera Mecarelli, L., Di Timoteo, G., Giuliani, A., D'Angelo, A., Santini, T., Perego, E., et al. (2024). ALS-associated FUS mutation reshapes the RNA and protein composition of stress granules. Nucleic Acids Res. *52*, 13269–13289. https://doi.org/10.1093/nar/gkae942.
20. Lam, S.S., Martell, J.D., Kamer, K.J., Deerinck, T.J., Ellisman, M.H., Mootha, V.K., and Ting, A.Y. (2015). Directed evolution of APEX2 for electron microscopy and proximity labeling. Nat. Methods *12*, 51–54. https://doi.org/10.1038/nmeth.3179.
21. Kaewsapsak, P., Shechner, D.M., Mallard, W., Rinn, J.L., and Ting, A.Y. (2017). Live-cell mapping of organelle-associated RNAs via proximity biotinylation combined with protein-RNA crosslinking. eLife *6*, e29224. https://doi.org/10.7554/eLife.29224.
22. Fazal, F.M., Han, S., Parker, K.R., Kaewsapsak, P., Xu, J., Boettiger, A.N., Chang, H.Y., and Ting, A.Y. (2019). Atlas of Subcellular RNA Localization Revealed by APEX-Seq. Cell *178*, 473–490.e26. https://doi.org/10.1016/j.cell.2019.05.027.
23. De Santis, R., Garone, M.G., Pagani, F., de Turris, V., Di Angelantonio, S., and Rosa, A. (2018). Direct conversion of human pluripotent stem cells into cranial motor neurons using a piggyBac vector. Stem Cell Res. *29*, 189–196. https://doi.org/10.1016/j.scr.2018.04.012.
24. Rotem, N., Magen, I., Ionescu, A., Gershoni-Emek, N., Altman, T., Costa, C.J., Gradus, T., Pasmanik-Chor, M., Willis, D.E., Ben-Dov, I.Z., et al. (2017). ALS Along the Axons – Expression of Coding and Noncoding RNA Differs in Axons of ALS models. Sci. Rep. *7*, 44500. https://doi.org/10.1038/srep44500.
25. Zappulo, A., van den Bruck, D., Ciolli Mattioli, C., Franke, V., Imami, K., McShane, E., Moreno-Estelles, M., Calviello, L., Filipchyk, A., Peguero-Sanchez, E., et al. (2017). RNA localization is a key determinant of neurite-enriched proteome. Nat. Commun. *8*, 583. https://doi.org/10.1038/s41467-017-00690-6.
26. Nijssen, J., Aguila, J., Hoogstraaten, R., Kee, N., and Hedlund, E. (2018). Axon-Seq Decodes the Motor Axon Transcriptome and Its Modulation in Response to ALS. Stem Cell Rep. *11*, 1565–1578. https://doi.org/10.1016/j.stemcr.2018.11.005.
27. Hafner, A.-S., Donlin-Asp, P.G., Leitch, B., Herzog, E., and Schuman, E.M. (2019). Local protein synthesis is a ubiquitous feature of neuronal pre- and postsynaptic compartments. Science *364*, eaau3644. https://doi.org/10.1126/science.aau3644.
28. Niu, M., Cao, W., Wang, Y., Zhu, Q., Luo, J., Wang, B., Zheng, H., Weitz, D.A., and Zong, C. (2023). Droplet-based transcriptome profiling of individual synapses. Nat. Biotechnol. *41*, 1332–1344. https://doi.org/10.1038/s41587-022-01635-1.
29. Bauer, K.E., Segura, I., Gaspar, I., Scheuss, V., Illig, C., Ammer, G., Hutten, S., Basyuk, E., Fernández-Moya, S.M., Ehses, J., et al. (2019). Live cell imaging reveals 3′-UTR dependent mRNA sorting to synapses. Nat. Commun. *10*, 3178. https://doi.org/10.1038/s41467-019-11123-x.
30. Mendonsa, S., von Kügelgen, N., Dantsuji, S., Ron, M., Breimann, L., Baranovskii, A., Lödige, I., Kirchner, M., Fischer, M., Zerna, N., et al. (2023). Massively parallel identification of mRNA localization elements in primary cortical neurons. Nat. Neurosci. *26*, 394–405. https://doi.org/10.1038/s41593-022-01243-x.
31. Chekulaeva, M. (2024). Mechanistic insights into the basis of widespread RNA localization. Nat. Cell Biol. *26*, 1037–1046. https://doi.org/10.1038/s41556-024-01444-5.
32. Van Nostrand, E.L., Freese, P., Pratt, G.A., Wang, X., Wei, X., Xiao, R., Blue, S.M., Chen, J.-Y., Cody, N.A.L., Dominguez, D., et al. (2020). A large-scale binding and functional map of human RNA-binding proteins. Nature *583*, 711–719. https://doi.org/10.1038/s41586-020-2077-3.
33. Todd, A.G., Morse, R., Shaw, D.J., Stebbings, H., and Young, P.J. (2010). Analysis of SMN-neurite granules: Core Cajal body components are absent from SMN-cytoplasmic complexes. Biochem. Biophys. Res. Commun. *397*, 479–485. https://doi.org/10.1016/j.bbrc.2010.05.139.
34. Francisco-Velilla, R., Fernandez-Chamorro, J., Dotu, I., and Martinez-Salas, E. (2018). The landscape of the non-canonical RNA-binding site of Gemin5 unveils a feedback loop counteracting the negative effect on

translation. Nucleic Acids Res. *46*, 7339–7353. https://doi.org/10.1093/nar/gky361.

35. Bilsland, L.G., Sahai, E., Kelly, G., Golding, M., Greensmith, L., and Schiavo, G. (2010). Deficits in axonal transport precede ALS symptoms in vivo. Proc. Natl. Acad. Sci. USA *107*, 20523–20528. https://doi.org/10.1073/pnas.1006869107.
36. Baldwin, K.R., Godena, V.K., Hewitt, V.L., and Whitworth, A.J. (2016). Axonal transport defects are a common phenotype in Drosophila models of ALS. Hum. Mol. Genet. *25*, 2378–2392. https://doi.org/10.1093/hmg/ddw105.
37. Kamelgarn, M., Chen, J., Kuang, L., Arenas, A., Zhai, J., Zhu, H., and Gal, J. (2016). Proteomic analysis of FUS interacting proteins provides insights into FUS function and its role in ALS. Biochim. Biophys. Acta Mol. Basis Dis. *1862*, 2004–2014. https://doi.org/10.1016/j.bbadis.2016.07.015.
38. Yasuda, K., Clatterbuck-Soper, S.F., Jackrel, M.E., Shorter, J., and Mili, S. (2017). FUS inclusions disrupt RNA localization by sequestering kinesin-1 and inhibiting microtubule detyrosination. J. Cell Biol. *216*, 1015–1034. https://doi.org/10.1083/jcb.201608022.
39. De Santis, R., Alfano, V., de Turris, V., Colantoni, A., Santini, L., Garone, M.G., Antonacci, G., Peruzzi, G., Sudria-Lopez, E., Wyler, E., et al. (2019). Mutant FUS and ELAVL4 (HuD) Aberrant Crosstalk in Amyotrophic Lateral Sclerosis. Cell Rep. *27*, 3818–3831.e5. https://doi.org/10.1016/j.celrep.2019.05.085.
40. De Pace, R., Ghosh, S., Ryan, V.H., Sohn, M., Jarnik, M., Rezvan Sangsari, P., Morgan, N.Y., Dale, R.K., Ward, M.E., and Bonifacino, J.S. (2024). Messenger RNA transport on lysosomal vesicles maintains axonal mitochondrial homeostasis and prevents axonal degeneration. Nat. Neurosci. *27*, 1087–1102. https://doi.org/10.1038/s41593-024-01619-1.
41. Martinez-Salas, E., Abellan, S., and Francisco-Velilla, R. (2025). Understanding GEMIN5 Interactions: From Structural and Functional Insights to Selective Translation. WIREs RNA *16*, e70008. https://doi.org/10.1002/wrna.70008.
42. Ciolli Mattioli, C., Rom, A., Franke, V., Imami, K., Arrey, G., Terne, M., Woehler, A., Akalin, A., Ulitsky, I., and Chekulaeva, M. (2019). Alternative 3′ UTRs direct localization of functionally diverse protein isoforms in neuronal compartments. Nucleic Acids Res. *47*, 2560–2573. https://doi.org/10.1093/nar/gky1270.
43. Lenzi, J., De Santis, R., de Turris, V., Morlando, M., Laneve, P., Calvo, A., Caliendo, V., Chiò, A., Rosa, A., and Bozzoni, I. (2015). ALS mutant FUS proteins are recruited into stress granules in induced Pluripotent Stem Cells (iPSCs) derived motoneurons. Dis. Model. Mech. dmm.020099. https://doi.org/10.1242/dmm.020099.
44. Schindelin, J., Arganda-Carreras, I., Frise, E., Kaynig, V., Longair, M., Pietzsch, T., Preibisch, S., Rueden, C., Saalfeld, S., Schmid, B., et al. (2012). Fiji: an open-source platform for biological-image analysis. Nat. Methods *9*, 676–682. https://doi.org/10.1038/nmeth.2019.
45. Martin, M. (2011). Cutadapt removes adapter sequences from high-throughput sequencing reads. EMBnet J. *17*, 10–12. https://doi.org/10.14806/ej.17.1.200.
46. Bolger, A.M., Lohse, M., and Usadel, B. (2014). Trimmomatic: a flexible trimmer for Illumina sequence data. Bioinformatics *30*, 2114–2120. https://doi.org/10.1093/bioinformatics/btu170.
47. Langmead, B., and Salzberg, S.L. (2012). Fast gapped-read alignment with Bowtie 2. Nat. Methods *9*, 357–359. https://doi.org/10.1038/nmeth.1923.
48. Dobin, A., Davis, C.A., Schlesinger, F., Drenkow, J., Zaleski, C., Jha, S., Batut, P., Chaisson, M., and Gingeras, T.R. (2013). STAR: ultrafast universal RNA-seq aligner. Bioinformatics *29*, 15–21. https://doi.org/10.1093/bioinformatics/bts635.
49. Anders, S., Pyl, P.T., and Huber, W. (2015). HTSeq—a Python framework to work with high-throughput sequencing data. Bioinformatics *31*, 166–169. https://doi.org/10.1093/bioinformatics/btu638.
50. Love, M.I., Huber, W., and Anders, S. (2014). Moderated estimation of fold change and dispersion for RNA-seq data with DESeq2. Genome Biol. *15*, 550. https://doi.org/10.1186/s13059-014-0550-8.
51. Yates, A.D., Achuthan, P., Akanni, W., Allen, J., Allen, J., Alvarez-Jarreta, J., Amode, M.R., Armean, I.M., Azov, A.G., Bennett, R., et al. (2019). Ensembl 2020. Nucleic Acids Res. *48*, gkz966. https://doi.org/10.1093/nar/gkz966.
52. Uhlén, M., Fagerberg, L., Hallström, B.M., Lindskog, C., Oksvold, P., Mardinoglu, A., Sivertsson, Å., Kampf, C., Sjöstedt, E., Asplund, A., et al. (2015). Tissue-based map of the human proteome. Science *347*, 1260419. https://doi.org/10.1126/science.1260419.
53. Quinlan, A.R., and Hall, I.M. (2010). BEDTools: a flexible suite of utilities for comparing genomic features. Bioinformatics *26*, 841–842. https://doi.org/10.1093/bioinformatics/btq033.
54. Drost, H.-G., and Paszkowski, J. (2017). Biomartr: genomic data retrieval with R. Bioinformatics *33*, 1216–1217. https://doi.org/10.1093/bioinformatics/btw821.
55. Gu, Z., Eils, R., and Schlesner, M. (2016). Complex heatmaps reveal patterns and correlations in multidimensional genomic data. Bioinformatics *32*, 2847–2849. https://doi.org/10.1093/bioinformatics/btw313.
56. Casper, J., Speir, M.L., Raney, B.J., Perez, G., Nassar, L.R., Lee, C.M., Hinrichs, A.S., Gonzalez, J.N., Fischer, C., Diekhans, M., et al. (2025). The UCSC Genome Browser database: 2026 update. Nucleic Acids Res. *54*, D1331–D1335, gkaf1250. https://doi.org/10.1093/nar/gkaf1250.
57. Bolte, S., and Cordelières, F.P. (2006). A guided tour into subcellular colocalization analysis in light microscopy. J. Microsc. *224*, 213–232. https://doi.org/10.1111/j.1365-2818.2006.01706.x.
58. Choi, H.M.T., Schwarzkopf, M., Fornace, M.E., Acharya, A., Artavanis, G., Stegmaier, J., Cunha, A., and Pierce, N.A. (2018). Third-generation in situ hybridization chain reaction: multiplexed, quantitative, sensitive, versatile, robust. Development *145*, dev165753. https://doi.org/10.1242/dev.165753.
59. Kuehn, E., Clausen, D.S., Null, R.W., Metzger, B.M., Willis, A.D., and Özpolat, B.D. (2022). Segment number threshold determines juvenile onset of germline cluster expansion in Platynereis dumerilii. J. Exp. Zool. Pt. B. *338*, 225–240. https://doi.org/10.1002/jez.b.23100.
60. Bahry, E., Breimann, L., Zouinkhi, M., Epstein, L., Kolyvanov, K., Mamrak, N., King, B., Long, X., Harrington, K.I.S., Lionnet, T., and Preibisch, S. (2022). RS-FISH: precise, interactive, fast, and scalable FISH spot detection. Nat. Methods *19*, 1563–1567. https://doi.org/10.1038/s41592-022-01669-y.

STAR★METHODS

KEY RESOURCES TABLE

REAGENT or RESOURCE	SOURCE	IDENTIFIER
Antibodies		
Anti-Beta III Tubulin, mouse monoclonal	Sigma-Aldrich	Cat# T8660; RRID:AB_477590
Anti-Beta III Tubulin, goat polyclonal	Thermo Fisher Scientific	Cat# PA5-142939; RRID:AB_2933581
Anti-CD63, mouse monoclonal	Thermo Fisher Scientific	Cat# 10628D; RRID:AB_2532983
Anti-DCP1a, mouse monoclonal	Santa Cruz Biotechnology	Cat# sc-100706; RRID:AB_2090408
Anti-EEA1, mouse monoclonal	Thermo Fisher Scientific	Cat# 14–9114-95; RRID:AB_2865350
Anti-FLAG®, rabbit polyclonal	Sigma-Aldrich	Cat# F7425; RRID:AB_439687
Anti-FLAG® M2, mouse monoclonal	Sigma-Aldrich	Cat# F3165; RRID:AB_259529
Anti-FUS, rabbit polyclonal	Bioss	Cat# bs-2980R; RRID:AB_11108028
Anti-GAPDH, mouse monoclonal	Santa Cruz Biotechnology	Cat# sc-47724; RRID:AB_627678
Anti-GEMIN5, rabbit polyclonal	Sigma-Aldrich	Cat# HPA037393; RRID:AB_10672489
Anti-GEMIN5, mouse monoclonal	Santa Cruz Biotechnology	Cat# sc-136200; RRID:AB_10839640
Anti-GFP, rabbit polyclonal	Thermo Fisher Scientific	Cat# A11122; RRID:AB_221569
Anti-Histone H3, rat monoclonal	Active Motif	Cat# 61647; RRID:AB_2687567
Anti-LAMP1, mouse monoclonal	DSHB	Cat# H4A3; RRID:AB_2296838
Anti-RAB5, mouse monoclonal	BD Biosciences	Cat# 610724; RRID:AB_398047
Anti-RAB7A, rabbit monoclonal	Abcam	Cat# ab137029; RRID:AB_2629474
Anti-TOM20, mouse monoclonal	Santa Cruz Biotechnology	Cat# sc-17764; RRID:AB_628381
Anti-V5, rabbit polyclonal	Novus	Cat# NB600-381; RRID:AB_10001084
Anti-V5, mouse monoclonal	Thermo Fisher Scientific	Cat# MA5-15253; RRID:AB_10977225
Anti-VINCULIN, rabbit polyclonal	Proteintech	Cat# 26520-1-AP; RRID:AB_2868558
Rabbit IgG Isotype control	Thermo Fisher Scientific	Cat# 02–6102; RRID:AB_2532938
Mouse IgG Isotype control	Thermo Fisher Scientific	Cat# 02–6100; RRID:AB_2532935
Bacterial and virus strains		
Stellar Competent Cells (*E. coli* HST08)	Takara	Cat# 636763
Chemicals, peptides, and recombinant proteins		
Biotin-Phenol	Iris Biotech	Cat# LS-3500
Sodium L-ascorbate	Sigma-Aldrich	Cat# A7631
TROLOX	Sigma-Aldrich	Cat# 238813
RPMI-1640 medium	Thermo Fisher Scientific	Cat# 31870025
Doxycycline hyclate	Sigma-Aldrich	Cat #D5207
Puromycin	Sigma-Aldrich	Cat# P4512
G418 disulfate	PanReach Applichem	Cat# A6798
Geltrex™ matrix	Thermo Fisher Scientific	Cat# A1413301
NutriStem® hPSC XF medium	Sartorius	Cat# 05-100-1A
NutriFreez® D10 Cryopreservation Medium	Sartorius	Cat# 05-713-1B
StemPro Accutase™ Cell Dissociation Reagent	Thermo Fisher Scientific	Cat# A1110501
Y-27632 dihydrochloride	Cayman Chemical	Cat# 10005583
Advanced DMEM/F-12 medium	Thermo Fisher Scientific	Cat# 12634010
Neurobasal™ medium	Thermo Fisher Scientific	Cat# 21103049
B-27™ supplement	Thermo Fisher Scientific	Cat# 17504044
DAPT	Sigma-Aldrich	Cat# D5942
SU-5402	Sigma-Aldrich	Cat# SML0443
Recombinant Human/Murine/Rat BDNF	Peprotech	Cat# 450–02
Human GDNF recombinant protein	Peprotech	Cat# 450–10

(*Continued on next page*)

Continued

REAGENT or RESOURCE	SOURCE	IDENTIFIER
Lipofectamine™ Stem Transfection Reagent	Thermo Fisher Scientific	Cat# STEM00003
Lipofectamine™ RNAiMAX Transfection Reagent	Thermo Fisher Scientific	Cat# 13778075
MISSION® esiRNA targeting human GEMIN5	Sigma-Aldrich	Cat# EHU049241
MISSION® esiRNA Universal Negative Control #1	Sigma-Aldrich	Cat# SIC001
PrimeScript RT Reagent Mix	Takara	Cat# RR037A
PowerUp™ SYBR™ Green Mastermix	Thermo Fisher Scientific	Cat# A25776
Ribolock RNase Inhibitor	Therno Fisher Scientific	Cat# EO0382
4–15% Mini-PROTEAN TGX Precast gels	Biorad	Cat# 4561086
Pierce™ 660 nm Protein Assay Reagent	Thermo Fisher Scientific	Cat# 22660
Immobilon Crescendo Western HRP Substrate	Sigma-Aldrich	Cat# WBLUR0500
Immobilon ECL UltraPlus Western HRP Substrate	Sigma-Aldrich	Cat# WBULP
Recombinant Proteinase K solution	Thermo Fisher Scientific	Cat# AM2546
Pierce™ Streptavidin Magnetic beads	Thermo Fisher Scientific	Cat# 88817
Dynabeads™ Protein G for Immunoprecipitation	Thermo Fisher Scientific	Cat# 10004D
Prolong™ Diamond Antifade Mountant	Thermo Fisher Scientific	Cat# P36961
Critical commercial assays		
NaveniFlex Cell MR RED kit	Navinci	Cat# 60025
Direct-zol™ Miniprep RNA Purification kit	Zymo	Cat# R2052
RNA Clean and Concentrator-5	Zymo	Cat# R1014
In-Fusion HD Cloning Kit	Takara	Cat# 630910
HCR™ (v3.0) RNA-FISH kit	Molecular Instruments	N/A
Stranded Total RNA Prep with Ribo-zero plus kit	Illumina	Cat# 20040529
Deposited data		
RAB7A-APEX2 pulldown RNA sequencing	This paper	GEO: GSE316825
Axon-seq and synaptic RNAs datasets	Rotem et al.[24]; Zappulo et al.[25]; Nijssen et al.[26]; Hafner et al.[27]; Niu et al.[28]	N/A ArrayExpress: E-MTAB-4978 GEO: GSE121069 BioProject: PRJNA544779 GEO: GSE199346
eCLIP datasets for RBPs	Van Nostrand et al.[32]	DCC: ENCSR456FVU
FUS^{WT}/FUS^{P525L} PAR-CLIP RNA sequencing	De Santis et al.[39]	GEO: GSE118347
Experimental models: Cell lines		
FUS^{WT}/FUS^{P525L} hiPSCs	Lenzi et al.[43]	N/A
SK-N-BE(2)	ATCC	CRL-2271
Oligonucleotides		
qPCR primers	This paper	Table S3
HCR FISH probes	This paper	Table S3
Recombinant DNA		
pBS L30 FLAG-APEX-RAB7A	Addgene	#135652
ePB NEO-EF1a-FLAG-APEX2-RAB7A	This paper	N/A
ePB BSD-EF1a-GEMIN5-V5	This paper	N/A
ePB NEO-EF1a-GFP-RAB7A	This paper	N/A
ePB NEO-EF1a-RLUC and related plasmids	This paper	N/A
Software and algorithms		
Fiji software	Schindelin et al.[44]	RRID: SCR_002285
NIS-Elements AR	Nikon	RRID: SCR_014329
Image Lab software	Biorad	RRID: SCR_014210
Prism 9	GraphPad by Dotmatics	https://www.graphpad.com/scientific-software/prism/

(*Continued on next page*)

Continued

REAGENT or RESOURCE	SOURCE	IDENTIFIER
QuantStudio 3 and 5 Real-Time PCR System Software	Thermo Fisher Scientific	RRID:SCR_020238
Cutadapt v3.2	Martin[45]	RRID:SCR_011841
Trimmomatic v0.39	Bolger et al.[46]	RRID:SCR_011848
Bowtie2 v2.4.2	Langmead and Salzberg[47]	RRID:SCR_016368
STAR v2.7.7a	Dobin et al.[48]	RRID:SCR_005622
HTSeq-count v0.13.5	Anders et al.[49]	RRID:SCR_011867
Picard MarkDuplicates v2.24.1	https://broadinstitute.github.io/picard	RRID:SCR_006525
DeSeq2 v1.34.0	Love et al.[50]	RRID:SCR_015687

EXPERIMENTAL MODEL AND STUDY PARTICIPANT DETAILS

Human cell lines

Isogenic iPSCs homozygous for either the FUS^{WT} or FUS^{P525L} alleles were kindly provided by Prof. A. Rosa. Cell lines were generated as previously described[43] and genetically engineered by random genomic integration of a cassette encoding the motor neuron transcription factors Ngn2-F2A-Isl1-T2A-Lhx3 (NIL) using an enhanced piggyBac transposable vector (epB-Bsd-TT-NIL). This system enables doxycycline-inducible differentiation into spinal motor neurons, as reported previously.[23]

SK-N-BE(2) cells (ATCC CRL-2271) engineered to express a FLAG-tagged version of FUS^{WT} or FUS^{P525L} were generated as in Mariani et al.[19]

Cells were routinely tested for mycoplasma contamination, and culture and manipulation conditions are described below.

METHOD DETAILS

Cell culture, maintenance and treatments

SK-N-BE cells were cultured in adherence in RPMI-1640 medium supplemented with 10% fetal bovine serum (FBS), sodium pyruvate (1 mM), GlutaMAX™ (1×), penicillin (100 U/mL), and streptomycin (100 μg/mL) (all from Thermo Fisher Scientific). For cryopreservation, cells were cryopreserved using a growth medium containing 20% FBS and 10% dimethyl sulfoxide (DMSO) and rapidly recovered when required by thawing in a 37°C water bath. FUS overexpression was induced by incubating cells with 50 ng/mL doxycycline hyclate (Sigma-Aldrich) for 24 h in culture medium. For GEMIN5 knockdown, cells were reverse transfected with 25 nM of either MISSION® esiRNA targeting human GEMIN5 (Sigma-Aldrich, EHU049241-20UG) or MISSION® esiRNA Universal Negative Control #1 (Sigma-Aldrich, SIC001, referred as "Scramble" in text and figures); Lipofectamine RNAiMAX Transfection Reagent (Thermo Fisher Scientific) was used for transfection, according to manufacturer's protocol.

Induced pluripotent stem cells (iPSCs) were maintained as adherent cultures on dishes coated with Geltrex™ matrix (1:100 dilution in serum-free medium; Gibco). Cells were cultured in NutriStem® hPSC XF medium (Sartorius) supplemented with penicillin (50 U/mL) and streptomycin (50 μg/mL) (Thermo Fisher Scientific). For cryopreservation, iPSCs were stored in NutriFreez® D10 Cryopreservation Medium and rapidly recovered by thawing in a 37°C water bath. Following thawing or enzymatic dissociation with Accutase (Thermo Fisher Scientific), cells were plated onto Geltrex™-coated dishes in complete culture medium supplemented with the ROCK inhibitor Y-27632 (10 μM; Cayman Chemical) for the first 24 h only to enhance cell survival. Colony morphology and growth were monitored daily by optical microscopy.

For APEX2-mediated proximity labeling experiments, iPSC-derived motor neurons were incubated in neuronal maintenance medium consisting of Neurobasal medium supplemented with B27, brain-derived neurotrophic factor (BDNF, 20 ng/mL), glial cell line–derived neurotrophic factor (GDNF, 10 ng/mL; both from PeproTech), and L-ascorbic acid (200 ng/mL; Sigma-Aldrich). Cultures were preincubated with biotin-phenol (1 mM; IRIS Biotech) for 1 h at 37°C, followed by a brief exposure to hydrogen peroxide (1 mM H_2O_2 in PBS) for 1 min to activate APEX2 and initiate biotinylation. The reaction was immediately quenched by two washes with a quenching buffer containing sodium ascorbate (10 mM) and Trolox (5 mM; Merck) in PBS.

Cloning and stable cell lines generation

Plasmid encoding N-terminal FLAG-APEX2–tagged human RAB7A was obtained from Addgene (plasmid #135652). FLAG-APEX2-RAB7A insert was subcloned into the ePB-NEO-EIF1a backbone downstream of the constitutive EIF1a promoter. Insert was PCR-amplified using CloneAmp HiFi PCR Premix (TakaraBio) and cloned into acceptor vector linearized by inverse PCR using the InFusion Cloning system (TakaraBio), following the manufacturer's guidelines for both reaction setup and primer design. To generate the GFP-tagged RAB7A, the FLAG-APEX2 coding sequence was excised from the ePB-NEO-EIF1a:FLAG-APEX2-RAB7A plasmid by inverse PCR and replaced with GFP. Cloning was performed using the InFusion Cloning system, yielding the ePB-NEO-EIF1a:GFP-RAB7A construct.

For RLUC constructs, the Renilla luciferase (RLUC) coding sequence was amplified from the psiCHECK2 plasmid (Promega) and cloned into the inverse-PCR–linearized ePB-NEO-EIF1a backbone using the InFusion Cloning system, generating the ePB-NEO-EIF1a:RLUC plasmid. To insert the 5′ untranslated region of endosome-*enriched*, *depleted* or *unspecific* mRNAs upstream of the RLUC coding sequence, the corresponding 5′UTR was amplified from cDNA derived from WT motor neurons used in this study and cloned into the ePB-NEO-EIF1a:RLUC construct according to the manufacturer's protocol, yielding ePB-NEO-EIF1a:5′UTR-RLUC plasmids. To establish stable iPSC lines, constructs were introduced via Lipofectamine™ Stem Reagent (Thermo Fisher Scientific), adhering to the transfection protocol recommended by the manufacturer. Successfully transfected cells were selected by neomycin resistance.

iPSCs differentiation into spinal motor neurons

Human iPSCs were cultured under standard maintenance conditions and enzymatically dissociated into single cells using Accutase (Thermo Fisher Scientific). Cells were seeded onto Geltrex™-coated culture surfaces (1:100 dilution in serum-free medium) at a density of 6.25×10^4 cells/cm^2 in NutriStem® hPSC XF medium (Sartorius) supplemented with penicillin (50 U/mL), streptomycin (50 μg/mL), and the ROCK inhibitor Y-27632 (10 μM). Twenty-four hours after plating, spinal motor neuron differentiation was initiated by doxycycline –mediated induction (1 μg/mL) in Advanced DMEM/F12 (Thermo Fisher Scientific) containing penicillin, streptomycin, and GlutaMAX™ (Thermo Fisher Scientific). Following 48 h of induction, cultures were transitioned to Neurobasal/B27 differentiation medium consisting of Neurobasal Medium supplemented with B27, GlutaMAX™, non-essential amino acids (NEAA), penicillin, and streptomycin (all from Thermo Fisher Scientific). This medium was further supplemented with doxycycline (1 μg/mL), the γ-secretase inhibitor DAPT (5 μM; Sigma-Aldrich), and the FGFR inhibitor SU5402 (4 μM; Sigma-Aldrich). On day 5 of differentiation, cells were dissociated again with Accutase and replated onto Geltrex™-coated dishes or glass coverslips at a density of 1×10^5 cells/cm^2. ROCK inhibitor (10 μM) was included for the first 24 h following replating to enhance cell survival. From day 5 onward, neuronal cultures were maintained in maturation medium composed of Neurobasal/B27 supplemented with brain-derived neurotrophic factor (BDNF, 20 ng/mL), glial cell line–derived neurotrophic factor (GDNF, 10 ng/mL; both from PeproTech), and L-ascorbic acid (200 ng/mL; Sigma-Aldrich). Cultures were maintained under these conditions until day 8, at which point cells were collected for downstream analyses.

RNA extraction and analysis

Total RNA was isolated using the Direct-zol™ Miniprep RNA Purification Kit (Zymo Research), including an on-column DNase digestion step, according to the manufacturer's instructions. RNA was eluted in 25 μL of RNase-free water. Reverse transcription was performed using the PrimeScript™ RT Reagent Kit (TakaraBio) following the supplier's protocol. Quantitative PCR (qPCR) was carried out using PowerUp™ SYBR™ Green Master Mix (Thermo Fisher Scientific) in 15 μL reaction volumes on a QuantStudio™ 5 Real-Time PCR System (Thermo Fisher Scientific), employing standard cycling parameters. For IP experiments, data were reported as percentage of input. Briefly, Ct values obtained from input samples were corrected for sample dilution by subtracting the $\log_2$ of the dilution factor. The percentage of input for each target transcript was subsequently calculated using the formula: % Input = 2 ^(Adjusted Input Ct−IP Ct). Primers used for qRT-PCR are listed in Table S3.

Protein extraction and analysis

Protein extracts for quantification of total protein levels were obtained using RIPA buffer (50 mM Tris-HCl pH 7.5, 150 mM NaCl, 0.1% SDS, 0.5% sodium deoxycholate, 1% Triton X-100, 5 mM EDTA), supplied with 1× Complete Protease Inhibitor Cocktail (Merck). Protein concentration was assessed by BCA assay or Pierce™ 660 nm protein assay (Thermo Fisher Scientific), according to the manufacturer's instructions. Protein electrophoresis was performed using 4–15% Mini-PROTEAN TGX Precast acrylamide gel (Bio-Rad), and proteins were transferred to 0,45 μm nitrocellulose membrane, using the TransBlot Turbo System (Bio-Rad), according to the manufacturer's protocol. Membranes were blocked with 5% non-fat dry milk (Sigma Aldrich) for 1 h and incubated with the following primary antibodies: anti-RAB7a (Abcam, AB137029, 1:1000), anti-LAMP1 (DHSB, H4A3, 1:1000), anti-GAPDH (Santa Cruz Biotechnology, sc-47724, 1:1000), anti-FLAG (Merck, F3165, 1:1000), anti-GEMIN5 (Sigma Aldrich, HPA037393, 1:500), anti-RAB5 (BD Transduction LaboratoriesTM, 610724, 1:1000), anti-H3 (Active motif, 616471:1000), anti-EEA1 (eBioscience, 14–9114, 1:1000), anti-TOM20 (Santa Cruz Biotechnology, sc-17764, 1:1000), anti-VINCULIN (ProteinTech, 26520-1-AP, 1:5000), anti-V5 (Thermo Fisher Scientific, MA5-15253, 1:1000). After secondary antibody incubation for 1 h at room temperature, protein detection was carried out either with Immobilon Crescendo Western HRP substrate (Merck)or Immobilon ECL UltraPlus Western HRP substrate using ChemiDoc™ MP System. Images were analyzed using Image Lab™ Software (Bio-Rad).

APEX2-pulldown of proteins and RNAs

APEX2-mediated pulldown was performed with modifications to the protocol described by Kaewsapsak et al.[21] Cells expressing APEX2 were cultured and treated as described above; control samples lacking peroxidase activation were processed in parallel without hydrogen peroxide exposure. Following biotinylation, cells were washed twice and fixed with 0.1% paraformaldehyde (PFA) in Quenching Buffer for 10 min. Residual PFA was quenched by addition of glycine to a final concentration of 125 mM, followed by incubation with gentle agitation at room temperature for 5 min. Cells were subsequently washed twice and lysed directly on the culture dish in complete RIPA buffer, supplemented with 1× Complete Protease Inhibitor Cocktail (Merck), 1× Ribolock RNase

Inhibitor (Thermo Fisher Scientific), 0.5 mM DTT, 10 mM sodium ascorbate (Merck) and 5 mM Trolox (Merck). Cell lysates were incubated under rotation at 4°C for 15 min and then sonicated on ice at 20% amplitude for 30 s (1 s on/1 s off), followed by a 30 s pause; this cycle was repeated three times per sample. Debris was removed by centrifugation at 15,000 × g for 5 min at 4°C. Protein concentration was determined as described above, and 200 μg of total protein per biological replicate was used for pulldown experiments. Samples were adjusted to a final volume of 200 μL with complete RIPA buffer, and 5% of each sample was reserved as input. 170 μL of NLB buffer (25 mM Tris-HCl pH 7.5, 150 mM KCl, 0.5% NP-40, 5 mM EDTA) supplemented with protease inhibitors (1× Complete Protease Inhibitor Cocktail, Merck), RNase inhibitor (1× Ribolock, Thermo Fisher Scientific), DTT (0.5 mM), and antioxidants (10 mM sodium ascorbate and 5 mM Trolox; Merck) were added to each sample. Streptavidin magnetic beads (40 μL; Pierce™, Thermo Fisher Scientific) were prewashed three times with binding and wash buffer (5 mM Tris-HCl pH 7.5, 1 M NaCl, 0.1% Tween 20, 0.5 mM EDTA), followed by two washes with a 1:1 mixture of RIPA and NLB buffers, and resuspended in the same buffer mixture. Beads were incubated with lysates for 2 h at 4°C under rotation (10 rpm). After binding, beads were washed eight times using buffers specified in the original protocol. For RNA-based downstream analyses, both pulldown and input samples were subjected to proteinase K digestion for 1 h at 42°C followed by an additional 1 h at 55°C. RNA was subsequently extracted using TRIzol™ LS (Thermo Fisher Scientific). For protein analyses, bound proteins were eluted after the final wash by incubation at 80°C for 10 min in 40 μL of elution buffer containing 1× Laemmli sample buffer (Bio-Rad), 50 mM DTT, and 2 mM free biotin (Merck).

Library preparation and RNA-seq analysis

RNA libraries were prepared using the Illumina Stranded Total RNA Prep with Ribo-Zero Plus kit and sequenced on an Illumina NovaSeq 6000 platform in paired-end mode, generating reads of 100 bases. Read quality was assessed with FastQC v0.11.9, which revealed a transient reduction in quality at the first base, residual contamination consistent with incomplete ribosomal RNA removal by Ribo-Zero Plus, and the presence of Illumina adapter sequences. Adapter trimming and removal of low-quality nucleotides were performed using cutadapt v3.2[45] with: *-u 1 -U 1 –trim-n –nextseq-trim = 20 -m 35* and Trimmomatic software v0.39[46] with PE mode and the following parameters; *ILLUMINACLIP:adapter_path:2:30:10:8:true LEADING:3 TRAILING:3 SLIDINGWINDOW:4:20 MINLEN:35*. To eliminate remaining ribosomal RNA, trimmed reads were aligned to an rRNA-only reference (Table S1) using Bowtie2 v2.4.2,[47] and only unmapped reads were retained. These filtered reads were subsequently aligned to the GRCh38 human genome using STAR[48] v2.7.7a with the following parameters: *–outSAMstrandField intronMotif –outSAMattrIHstart 0 –outSAMtype BAM SortedByCoordinate –outFilterType BySJout –outFilterMultimapNmax 20 –alignSJoverhangMin 8 –alignSJDBoverhangMin 1 –outFilterMismatchNmax 999 –outFilterMismatchNoverLmax 0.04 –outFilterIntronMotifs RemoveNoncanonical –readFilesCommand zcat –outReadsUnmapped Fastx –peOverlapNbasesMin 35 –alignEndsType EndToEnd*. Because pull-down–derived RNA libraries typically undergo additional PCR amplification, PCR duplicates were removed using Picard MarkDuplicates v2.24.1(https://broadinstitute.github.io/picard/), and then gene level quantifications were performed with HTSeq-count[49] v0.13.5 using Ensembl GTF gene annotation related to release 99[51] and these parameters: *-s reverse -m union -t exon*. Read counts at each processing stage are summarized in the accompanying prospect (Table S1). Enrichment between biotin pull-down and input samples was evaluated using DESeq2[50] v1.34.0. Only transcripts with at least 1 average FPKM in input were kept for the analysis. To account for variability stemming from independent iPSC-to-motor neuron differentiation batches, each differentiation date was included as a batch factor in the DESeq2 design. Transcripts were classified as enriched when displaying a $\log_2$ fold change greater than 0.59 with an adjusted p value below 0.05, and as depleted when the $\log_2$ fold change was lower than −0.59 with an adjusted p value below 0.05. Transcripts not meeting these criteria were considered unspecific. This procedure was applied to both RAB7 H_2O_2–treated samples and the corresponding –H_2O_2 controls. APEX-seq experiments were carried out in parallel under FUS^{WT} and FUS^{P525L} conditions. The dataset produced in iPSC-derived MN with WT genotype was used as the reference to describe the endosomal RNA localisation landscape under physiological conditions.

RBP binding enrichment analysis

To identify RNA-binding proteins (RBPs) preferentially associated with the 5′UTRs of endosomal transcripts compared to depleted RNAs, we analyzed enhanced crosslinking and immunoprecipitation (eCLIP) datasets from K562 and HepG2 cells.[32] Of 150 profiled RBPs, those annotated as nuclear or with uncertain localization were excluded based on the Human Protein Atlas[52] subcellular localization dataset (https://www.proteinatlas.org/humanproteome/subcellular/data#locations), yielding 49 cytoplasmic RBPs for downstream analyses. Endosome-enriched and depleted RNA sets were defined by enrichment analysis and restricted to protein-coding genes expressed in motoneurons, K562, and HepG2 cells. Genomic coordinates for 5′UTRs were extracted from Ensembl gene annotation release 99. Strand-specific intersections between RBP eCLIP peaks and 5′UTRs were performed using BEDTools v2.29.1[53] to identify RBP–transcript interactions. For each RBP, transcripts with overlapping peaks on 5′UTR were classified as interacting, while transcripts lacking overlaps on their 5′UTR were considered non-interacting. Statistical significance of RBP binding enrichment to 5′UTRs of endosome-enriched versus depleted transcripts was assessed using Fisher's exact tests. p values were corrected for multiple testing using false discovery rate (FDR) adjustment, and RBPs with FDR <0.05 and log2Odds Ratio >1 were considered preferentially interacting with the 5′UTR of endosomal RNAs (Table S2). To assess 5′UTR specificity relative to coding sequence (CDS) and 3′UTR regions, we took advantage of metatranscript profile generated based on the lengths of the 5′UTR, CDS or 3′UTR regions of the expressed transcripts (FPKMs >1). This information, together with the transcript sequences were retrieved from the Ensembl 99 database using the biomartR package v.2.50.3.[54] Each mRNA region was divided into an equal

number of bins, ensuring the proportions among the lengths of the transcript's regions were maintained. The bin ranges for each RNA were compiled into a BED file, and the sequences for each bin were extracted using BEDTools getfasta from the transcriptome FASTA file. For each RBP, their profiles were calculated based on the frequencies of interacting bins followed by *Z* Score normalization. Graphical representations of meta-region and meta-transcript analyses were performed using ComplexHeatmap R package v2.10.0.[55]

Conservation analysis

To assess evolutionary conservation of 5′UTRs in endosomal transcripts, we analyzed phylogenetic conservation scores across transcript regions. Longest isoform of protein-coding transcripts were selected, according to the ensemble annotation release 99. Transcript lengths were used to generate consecutive, non-overlapping 50-nt bins spanning full transcript bodies using BEDTools makewindow version 2.29.1. Transcript bins were annotated as 5′UTR, CDS, or 3′UTR and mapped to genomic coordinates in a strand-specific manner. Conservation scores were extracted for each bin using the BigWig file of phyloP100-way vertebrate conservation scores retrieved from UCSC[56] golden path (https://hgdownload.cse.ucsc.edu/goldenpath/hg38/phyloP100way/), and mean phyloP scores were assigned per bin. Conservation scores were compared between 5′UTR and 3′UTR regions. Statistical differences in conservation between enriched and depleted transcript groups were assessed using the Mann–Whitney U test.

Localization analysis

To determine whether endosome-enriched transcripts were also enriched in axonal or synaptic localization datasets, we compared our endosomal RNA-seq dataset against publicly available axonal and synaptic transcriptome datasets. Axon-enriched transcripts were derived from three sources: a human motor neuron axonal transcriptome from Nijssen et al.[26] (axon vs. soma differential expression; log2FC > 1, padj <0.05) and two mouse datasets.[24,25] Since the latter two datasets were generated in mice, gene identifiers were mapped to human orthologs using the biomartR package v2.50.3. The union of the three gene lists defined the axonal gene set. Synapse-enriched transcripts were derived from two publicly available datasets,[27,28] and their union defined the synaptic gene set. Each endosomal transcript was flagged as axonal or synaptic based on membership in the respective gene sets described above. For each localization category, a 2 × 2 contingency table was constructed comparing localization membership (in-set vs. not in-set) with endosomal enrichment status, and statistical significance of the association was assessed using a two-tailed Fisher's exact test, yielding an odds ratio and *p*-value for each category. Percentages of enriched and depleted transcripts within the axonal and synaptic sets were calculated and displayed as bar plots.

Immunofluorescence analysis

Cells were fixed with 4% paraformaldehyde for 10 min at room temperature, followed by three washes with PBS. Membrane permeabilization was achieved by incubating coverslips in PBS containing 0.05% Triton X-100 for 5 min at room temperature. Non-specific binding was blocked by incubation in PBS supplemented with 2% bovine serum albumin (BSA) for 30 min at room temperature. Coverslips were then incubated for 1 h at RT with primary antibodies diluted in PBS containing 1% BSA. The following primary antibodies were used: anti-RAB7A (Abcam, ab137029; 1:250), anti-LAMP1 (DHSB, H4A3; 1:500), anti-FLAG (Merck, F3165; 1:500), anti-FLAG (Merck, F7425, 1:500), anti-GEMIN5 (Santa Cruz Biotechnology, sc-136200, 1:250), anti-DCP1a (Santa Cruz Biotechnology, sc-100706, 1:250), anti-CD63 (Invitrogen, 10628D, 1:250). After three washes in PBS (5 min each), samples were incubated for 45 min at room temperature with fluorophore-conjugated secondary antibodies (Thermo Fisher Scientific) diluted 1:300 in PBS containing 1% goat or donkey serum. Following secondary antibody incubation, coverslips were washed three times with PBS and nuclei were counterstained with DAPI (1 μg/mL in PBS; Sigma-Aldrich) for 3 min at room temperature. Coverslips were mounted onto microscope slides using ProLong™ Diamond Antifade Mountant (Thermo Fisher Scientific). Imaging was performed using a Nikon A1 confocal laser-scanning microscope equipped with 60× and 100× objectives. z stack images were acquired using the NIS-Elements AR software (Nikon) with the ND Acquisition module, using a Z-step size of 150–175 nm. Image analysis was conducted using FIJI/ImageJ open-source software.[44] For colocalization analysis, nuclear regions were segmented based on the DAPI signal and excluded to restrict analyses to the cytoplasmic compartment. After Gaussian blur filtering and background subtraction, Pearson's correlation coefficient was calculated on Maximum Intensity Projections using the JaCoP plugin.[57] For particle count analysis, after Gaussian blur filtering and background removal, the analyze particles function was used and SOMA vesicles were identified by enlarging the mask of nuclei on the Maximum Intensity Projections of Z-planes. 3D details were produced using the 3D volume viewer plugin of Fiji software.

Single-molecule fluorescence *in situ* hybridization analysis

RNA-FISH staining was carried out using the HCR RNA-FISH technology[58] according to manufacturer protocol (https://www.molecularinstruments.com/hcr-rnafish), with minor modifications to improve simultaneous RNA and protein visualization. HCR probes targeted to the RNAs of interest and compatible with the B3 amplifier were designed using the Özpolat Lab HCR probe generators.[59] Probe sequences are available in Table S3. Imaging was performed as specified above. FIJI/ImageJ open-source software was used to analyze images. Colocalization analyses were carried out excluding nuclear regions as previously indicated. Gaussian blur filtering and background subtraction were applied before merging all Z-stacks with maximum intensity projection. RS-FISH plugin[60] was used for RNA FISH spot detection. The % of FISH spot colocalization was calculated with the JaCoP plug-in tool. Digital

enlargements were obtained by manual cropping from original full-field images. 3D details were produced using the 3D volume viewer plugin of Fiji software. For FISH spot quantification in neurites related to Figure 5D, TUBBIII signal detected by anti-Beta III Tubulin (Sigma-Aldrich, T8660, 1:200) was utilized to define the cellular area and exclude extracellular noise. FISH spots were quantified as specified above and the final results were expressed as the number of FISH spots per analyzed cellular area.

Proximity Ligation Assay (PLA) and analysis

PLA experiments were carried out using the NaveniFlex Cell MR RED kit (Navinci) according to manufacturer protocol. Anti-RAB7A (Abcam, ab137029; 1:250), anti-GEMIN5 (Santa Cruz Biotechnology, sc-136200, 1:250), and anti-FUS (Bioss, bs-2980R, 1:250) were used as primary antibodies. Imaging was performed as described above. FIJI/ImageJ open-source software was used to analyze images. The Beta III Tubulin signal was utilized to define the cellular area and exclude extracellular noise. Gaussian blur filtering and background subtraction were applied to the PLA signal before merging all Z-stacks with maximum intensity projection. PLA spots were quantified with ''Analyze Particles'' tool and the final results were expressed as the number of PLA spots per cell area.

UV-crosslinked immunoprecipitation (CLIP)

5×10^6 SK-N-BE cells were seeded in a 15 cm plate. Cells were cultured for two days and UV-crosslinked on ice at 150 mJ/cm^2, then collected by scraping in PBS and flash-frozen in dry ice. Pellets were lysed in CLIP Lysis Buffer (20 mM TRIS-HCl pH 7.5, 150 mM NaCl, 5 mM MgCl2, 0,5% NP-40, 0.5 mM DTT, 1× Protease Inhibitory Cocktail and 1:300 Ribolock (Thermo Fisher Scientific) by incubation for 10 min on ice, and lysates were homogenized through sonication at 25% amplitude for 5 pulses (2 s on/2 s off), followed by a 30s pause; this cycle was repeated four times per sample. Lysates were cleared by centrifugation at 15000*g*, 10 min, 4°C. After BCA quantification, 500 μg of lysate were combined with 2 μg of anti-V5 antibody (Novus Biologicals, NB600-381) or control IgGs (Thermo Fisher, 02–6102), and incubated for 2:30 h at 4°C in a final volume of 500 μL. Antibody-protein complexes were recovered by adding 50 μL of Dynabeads Protein G magnetic beads (Thermo Fisher Scientific) and incubating for 1 h at 4°C. Beads were washed thrice in 1 mL of Wash Buffer (20 mM TRIS-HCl pH 7.5, 250 mM NaCl, 1mM MgCl2, 0,5% NP-40). ¾ of beads were treated with 100 μg of Proteinase K (Thermo Fisher Scientific, AM2546) in PK Buffer (75 mM TRIS-HCl pH 7.5, 10 mM EDTA, 0,1% SDS) for 1 h at 42°C; the reaction was stopped by adding 5 volumes of TRIZOL LS Reagent (Thermo Fisher Scientific). The remaining ¼ of beads were used for protein elution by boiling in 1× Laemmli Sample Buffer, 50 mM DTT for 15 min at 90°C.

Co-immunoprecipitation

5×10^6 SK-N-BE cells were seeded in two 15 cm plates per sample. Cells were cultured for two days, collected by scraping in PBS and flash-frozen in dry ice. Pellets were lysed in 400 μL of Co-IP Buffer (1× PBS, 0.01% NP-40, 1× Protease Inhibitory Cocktail) on ice for 10 min, and lysates were homogenized by passing 10 times through a 26G needle. Lysates were cleared by two rounds of centrifugation at 5000*g*, 10 min, 4°C to obtain a cytoplasm-enriched fraction. After BCA quantification, 1 mg of lysate was combined with 50 μL of Dynabeads Protein G magnetic beads (Thermo Fisher Scientific) previously coupled with 2 μg of anti-V5 antibody (Novus Biologicals, NB600-381) or control IgGs (Thermo Fisher, 02–6102), and incubated for 4 h at 4°C in a final volume of 500 μL. Beads were washed thrice with 1 mL of Co-IP buffer in rotation for 5 min at 4°C, and proteins were eluted by boiling in 1× Laemmli Sample Buffer, 50 mM DTT for 15 min at 90°C.

QUANTIFICATION AND STATISTICAL ANALYSIS

Statistical analyses were performed using R (v 4.4.0) and GraphPad Prism (v 9). Sample size and description (n), statistical tests used, center and dispersion measures, significance measures are reported in figure legends. All thresholds that were set for transcripts categorization are reported in the dedicated method details sections.